



Original Paper

Evolution process and controlling factors of gas content in marine–continental transitional shales: Insights from numerical modeling



Xiao-Guang Yang^{a,b,c,*}, Shi-Zhen Li^{b,**}, Qiu-Chen Xu^{b,d}, Fei Li^d, Xiang-Lin Chen^d

^a State Key Laboratory of Shale Oil and Gas Enrichment Mechanisms and Efficient Development, Beijing, 102206, China

^b State Key Laboratory of Continental Shale Oil, Oil and Gas Survey, Beijing, 100083, China

^c Petroleum Exploration and Production Research Institute, SINOPEC, Beijing, 102206, China

^d Oil and Gas Survey, China Geological Survey, Beijing, 100083, China

ARTICLE INFO

Article history:

Received 26 May 2025

Received in revised form

14 July 2025

Accepted 6 January 2026

Available online 12 January 2026

Edited by Xi Zhang and Jie Hao

Keywords:

Shale gas

Marine-continental transitional facies

Gas content model

Evolutionary process

Controlling factors

ABSTRACT

Marine-continental transitional shale (MCTS) gas holds excellent gas-generating hydrocarbon basis and exploration potential. Conducting quantitative analysis on the evolution of shale gas content and the coupled relationship between hydrocarbon generation and storage during geological history is essential for a profound understanding of shale gas enrichment mechanisms. This study establishes integrated models for hydrocarbon generation evolution, porosity evolution, and gas occurrence in Type III organic-rich MCTS through a synergistic experimental approach combining multi-temperature methane isothermal adsorption experiments and gold-tube pyrolysis experiments on low-maturity shale samples. Simulating a variety of real and virtual burial histories and thermal histories, the evolution process of gas content in MCTS was reconstructed and the influence of various geological conditions during burial on gas content evolution was clarified. The results indicate that a seven-stage evolution (A–G) of gas content in MCTS from the Shanxi Formation, Southern North China Basin. Critical thresholds include: (1) dissolution-enhanced reservoir modification at vitrinite reflectance ($EasyR_o$) = 1.0%, (2) adsorbed gas saturation at $EasyR_o$ = 1.3%, (3) dual saturation of free and adsorbed gas at $EasyR_o$ = 2.0%, (4) 15%–30% gas loss through expulsion during overmature stages ($EasyR_o > 2.0\%$), and (5) partial free-to-adsorbed gas conversion triggered by tectonic uplift. Total organic carbon (TOC) content and over-pressure exhibit positive correlations with gas content, while tectonic uplift magnitude shows a negative impact. The influence of maximum burial depth, paleo-heat flow, and geothermal gradient demonstrate complex nonlinear relationships on gas content.

© 2026 The Authors. Publishing services by Elsevier B.V. on behalf of KeAi Communications Co. Ltd. This is an open access article under the CC BY-NC-ND license (<http://creativecommons.org/licenses/by-nc-nd/4.0/>).

1. Introduction

Shale oil and gas have been globally recognized as abundant unconventional hydrocarbon resources (Curtis, 2002; Jarvie et al., 2007; Guo et al., 2025). Over the past decade, successful exploration cases have emerged from various marine shale formations

including the Barnett Shale in the Fort Worth Basin (Loucks et al., 2009), the Woodford Shale in Oklahoma and Texas, the Horn River Group shale in the western Canada Basin (Dong et al., 2015), as well as the Posidonia Shale in Europe, and the Longmaxi Formation shales in the Sichuan Basin (Tian et al., 2016; Yang et al., 2016; Zou, 2024). These formations are characterized by Type I and II kerogen-rich marine shales. However, MCTS containing predominantly Type III kerogen have not yet yielded commercially viable reserves on an industrial scale (Lu et al., 2024). Recent studies suggest these MCTS possess unique hydrocarbon enrichment mechanisms that warrant further investigation.

The inherent advantage of in-situ hydrocarbon accumulation in shale reservoirs makes the reservoir space characteristics

* Corresponding author.

** Corresponding author.

E-mail addresses: yangxiaoguang1993@126.com (X.-G. Yang), lishz2006@sina.com (S.-Z. Li).

Peer review under the responsibility of China University of Petroleum (Beijing).

(including pore distribution, architecture, wettability, and connectivity) critical determinants of hydrocarbon enrichment and production efficiency (Yang et al., 2019; Nie et al., 2024). In contrast, conventional reservoir evaluation based solely on present-day observable properties proves inadequate, as preservation conditions and the historical evolution of source-reservoir systems fundamentally govern the effective accumulation of generated hydrocarbons (Han et al., 2017).

The evolution process of shale gas is a critical and challenging topic, with the coupling relationship between hydrocarbon generation and storage being the core issue of shale gas evolution research (Guo et al., 2024). Within China's transitional facies, coal-bearing shales dominated by Type III kerogen exhibit distinct hydrocarbon generation characteristics compared to their marine and lacustrine counterparts (Xin et al., 2023). These organic-rich deposits demonstrate exceptional gas-generating potential coupled with elevated TOC, but suffer from suboptimal hydrocarbon conversion efficiency. The frequent changes in water bodies and climate in transitional facies also result in rapid vertical variation in organic matter content.

For reservoir formation mechanisms, MCTS are rich in clay minerals, which form numerous intercrystalline and intergranular pores (Lis et al., 2025). The transformation and compression of clay minerals during burial and diagenesis have a significant impact on the porosity (Xie et al., 2022; Yu et al., 2022). Compared to marine shales, Type III organic matter, predominantly comprising terrestrial plant fragments, exhibits significantly fewer organic matter pores but commonly shows organic matter shrinkage fractures (Zhang et al., 2025). Since shale gas exists mainly as adsorbed gas and free gas, which differ greatly in density underground, it is essential to analyze the changes in their occurrence states during shale gas evolution. It is widely believed that shale gas occurs mainly as adsorbed gas in shallow strata (<2000 m) and gradually turns into predominantly free gas in the middle and deep strata (2000–6000 m) (Borjigin et al., 2021). However, quantitative research on the evolution of gas content in MCTS during geological history is still relatively scarce. Understanding the evolution process and controlling factors of gas content in MCTS is crucial for a deeper understanding of shale gas enrichment mechanisms and guiding future exploration efforts (Li et al., 2022; Zhang et al., 2022).

This study employs methane isothermal adsorption experiments and gold-tube pyrolysis simulations under geological formation conditions. By integrating the Logistic model, hydrocarbon generation potential model, multi-porosity model, Langmuir model, and high-precision supercritical methane density, we comprehensively establish models for hydrocarbon generation, reservoir space, and gas occurrence mechanisms in MCTS. Basin-scale numerical simulation is implemented to reconstruct the evolution process of gas content in MCTS. Through the establishment of various virtual burial processes, we clarify the influence of different geological conditions during burial on the evolution of gas content.

2. Geological setting

The Permian organic-rich MCTS are widely developed across tectonic units in North and South China, with the Southern North China Basin and western Guizhou being typical representatives (Fig. 1(a)). The Southern North China Basin is located in the southern margin of the North China Craton and, under the control of an Early Permian marine-continent transitional environment (Yang and Guo, 2021), hosts organic-rich shales represented by the Shanxi Formation (Fig. 1(b)). Concurrently, the western Guizhou area along the southwestern margin of the Upper Yangtze Block

witnessed intense marine-terrestrial interactions during the Middle Permian Longtan Stage, resulting in the deposit (Fig. 1(c)). These two regions not only constitute crucial exploration targets for Permian MCTS gas resources in China but also exhibit distinctive hydrocarbon generation potential and gas-bearing evolutionary characteristics.

The Shanxi Formation in the Southern North China Basin and Longtan Formation shales in western Guizhou, both belonging to the Permian marine-continent transitional sedimentary system of South China, exhibit similar characteristics in organic matter type (predominantly Type III kerogen), sedimentary microfacies (delta-tidal flat), and diagenetic evolution pathways (Hu et al., 2023; Li and Guo, 2023): (1) both developed transgressive systems tracts during the global Permian sea-level fall, characterized by prolonged water retention and suboxic-anoxic bottom water conditions conducive to organic enrichment; (2) the depositional environments were both controlled by marine-continent transitional facies, where the coupling between clastic supply and biological productivity fostered the formation of shale strata enriched in Type III kerogen; (3) tectonically situated within craton marginal depression belts, they acquired similar uplift-depression architectures through later tectonic modification, ultimately yielding analogous shale pore structures.

Samples from the Shanxi Formation of Well Y23 in the Southern North China Basin (depth: 1421.9 m, $R_o = 0.95\%$) were conducted on thermal simulation experiments. The relatively low maturity ($R_o < 1.0\%$) of these samples is beneficial for capturing the gas generation characteristics during the middle to late stages of organic matter thermal evolution. Shale samples from Well Y24 in the Longtan Formation of the western Guizhou region (depths: 1110.2–1275.5 m, $R_o = 2.54\%$ – 2.71% , TOC = 2.83%–5.75%) were used for methane isothermal adsorption experiments (Yang and Guo, 2022). These samples have moderate maturity and TOC gradient, enabling the analysis of the control effect of organic matter content on shale adsorbed gas content (Table 1).

3. Experimental methods and results

3.1. Methane isothermal adsorption experiment

Four organic-rich shale samples from the Permian transitional facies with different TOC values are selected for multi-temperature methane isothermal adsorption experiments (Table 1, Y24-31, Y24-50, Y24-56, Y24-61). The experiments are conducted using a GAI-100 high-pressure gas isotherm adsorption analyzer by Core Lab, USA (Chen et al., 2019). This system features a maximum operating pressure of 68 MPa and temperature range of 0–177 °C, with a precision pressure transducer (accuracy: ± 0.1 MPa) and Pt100 resistance thermometer (accuracy: ± 0.2 °C) for real-time monitoring.

Each sample undergoes methane isothermal adsorption experiments at 20, 27.5, 40, 52.5, and 65 °C, with a pressure range from 0 to 30 MPa. 5 g shale sample with an approximate grain size of 80 mesh is placed in a drying oven and dried at 110 °C for 48 h. After drying, the sample is placed in a drying dish, and K_2SO_4 solution with a relative humidity of 97% is placed at the bottom of dish for humidity equilibrium treatment (Merkel et al., 2016), which is maintained for 72 h to simulate in-situ moisture conditions. Prior to the formal experiment, helium (99.999% purity) is used to calibrate the dead volume of the sample cell and connecting pipelines using an AJP-100 calibrator by Core Lab, USA, with 5 replicate measurements to ensure the relative error of dead volume is < 2% (Hu et al., 2022). During the test, methane gas with a purity of 99.99% is injected into the reference cell, and the pressure equilibrium is determined when the pressure fluctuation

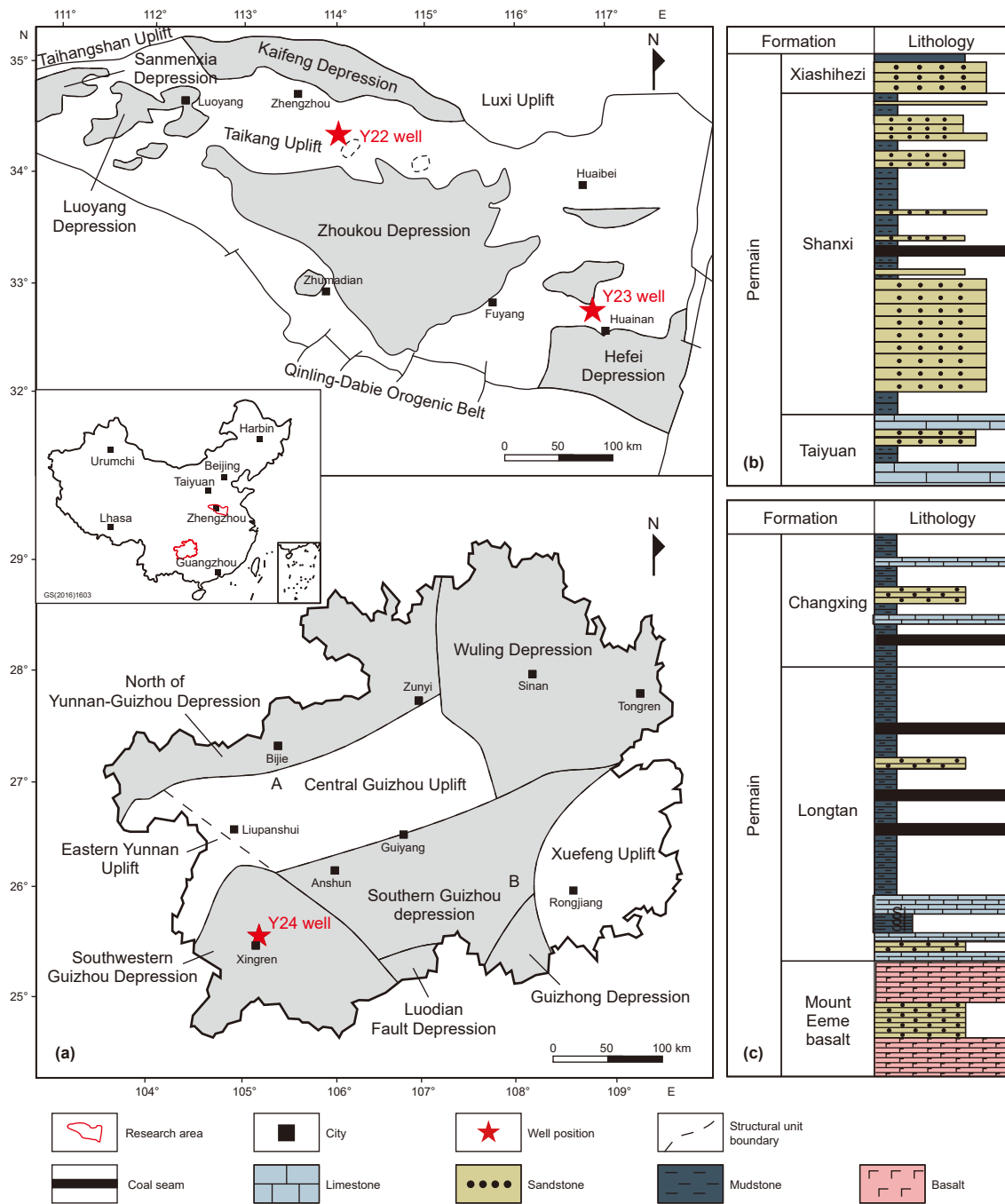


Fig. 1. (a) Structural unit division and well locations in the Southern North China Basin and Guizhou region of China; (b) lithologic column diagram of the Permian Shanxi Formation transitional facies in the Southern North China Basin; (c) lithologic column diagram of the Permian Longtan Formation transitional facies in the western Guizhou region.

Table 1
Basic information of experimental samples.

Samples ID	Depth, m	TOC, %	R _o , %	Kerogen type	Region	Formation
Y24-31	1110.2	2.83	2.54	III	Western Guizhou	Longtan
Y24-50	1219.6	4.87	2.65	III		
Y24-56	1248.5	5.75	2.68	III		
Y24-61	1275.5	4.16	2.71	III		
Y23-3	1421.9	1.55	0.95	III	Southern North China Basin	Shanxi

is < 0.01 MPa within 30 min. At each temperature point, 8 pressure points and the corresponding adsorbed gas amounts are measured. The adsorbed gas amount is calculated using the volumetric method based on the ideal gas law, corrected for real gas behavior using the compressibility factor from the National Institute of Standards and Technology (NIST) Chemistry WebBook (<http://webbook.nist.gov/chemistry/fluid>). The classic Langmuir equation is used to describe the methane adsorption behavior (Yang and Guo, 2022; Li et al., 2025):

$$V = \frac{P \times V_L}{P + P_L} \tag{1}$$

In the equation, V is methane volume at STP, cm^3/g ; P is current pressure, MPa; V_L is Langmuir volume, which represents the maximum adsorption volume that sample can reach, cm^3/g ; P_L is the Langmuir pressure, which represents the pressure at which adsorption amount reaches half of V_L , MPa.

By fitting the experimentally measured data after absolute adsorption correction, it is found that this model provided a good fit for methane isothermal adsorption data under different temperature conditions (Fig. 2). The V_L ranges from 1.69 to 3.34 cm^3/g , and P_L ranges from 1.37 to 2.41 MPa. The R^2 (correlation coefficients) ranges from 0.95 to 0.99 (Table 2).

3.2. Thermal simulation and rock pyrolysis experiments

Thermal simulation experiments are an essential method for hydrocarbon source rocks evolution. Thermal simulation experiments are categorized into closed, semi-open, and open systems. In this study, a closed system hydrothermal method is employed (Xie et al., 2014) at the State Key Laboratory of Environmental

Table 2
Fitting results and parameters of Langmuir model for test samples.

Samples ID	Temperature, °C	Parameter		
		V_L , cm^3/g	P_L , MPa	R^2
Y24-31	20	2.59	1.49	0.99
	27.5	2.47	1.7	0.96
	40	2.26	1.84	0.96
	52.5	2.01	2.07	0.98
	65	1.69	2.22	0.98
Y24-50	20	3.34	1.37	0.99
	27.5	3.15	1.52	0.97
	40	2.99	1.7	0.98
	52.5	2.7	1.93	0.99
	65	2.6	2.2	0.99
Y24-56	20	3.54	1.39	0.96
	27.5	3.24	1.51	0.95
	40	3.1	1.71	0.99
	52.5	2.77	2.24	0.98
	65	2.35	2.41	0.98
Y24-61	20	3.21	1.34	0.99
	27.5	3.09	1.54	0.96
	40	2.82	1.8	0.96
	52.5	2.6	1.98	0.98
	65	2.38	2.15	0.99

Geochemistry (SKLEG), Guangzhou Institute of Geochemistry, Chinese Academy of Sciences, where half the mass of sample is mixed with distilled water in the gold tube to supplement the water consumed during pyrolysis. Firstly, 20 g of low-maturity transitional facies shale samples (Table 1, Y23-3) are ground to a grain size of 10–15 mesh, mixed thoroughly, and divided into 10 sub-samples of 2 g each for thermal simulation experiments at different temperatures. The sub-samples are placed in gold tubes

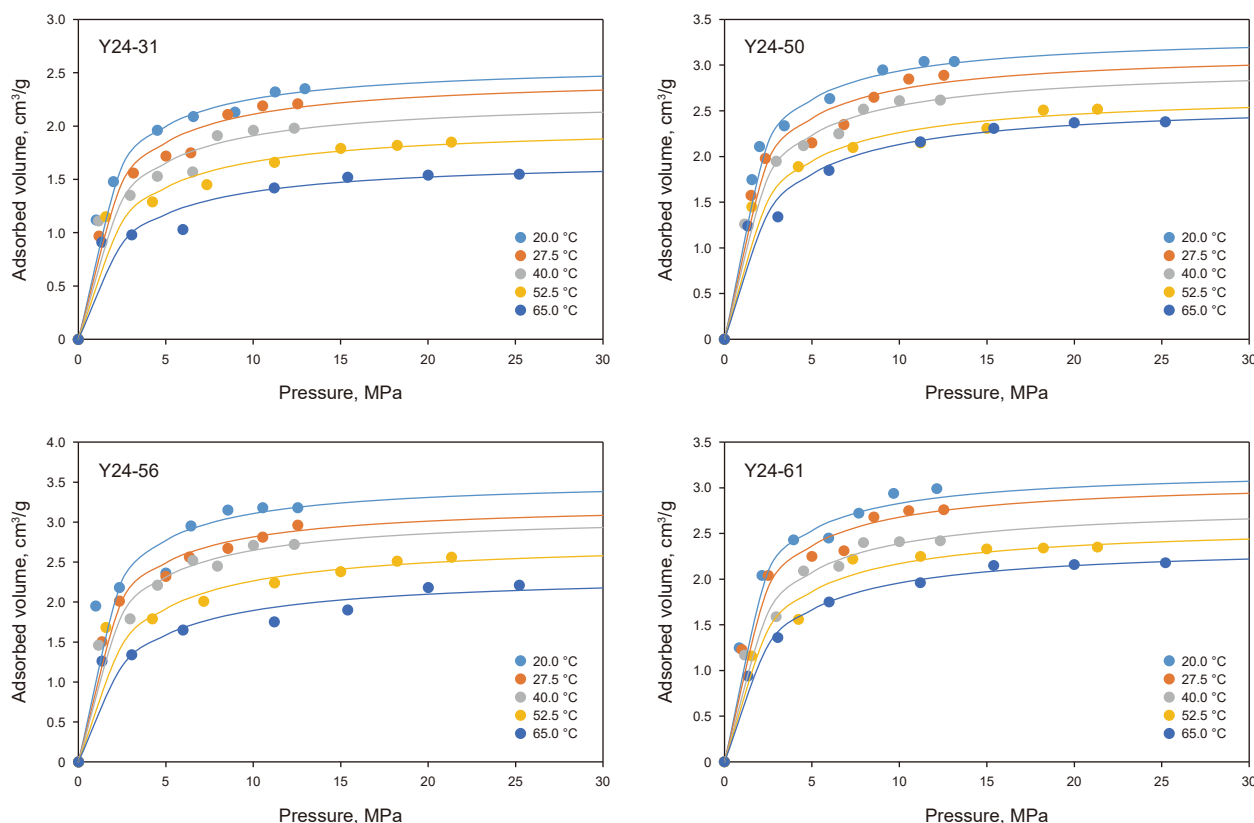


Fig. 2. Methane adsorption characteristics of shale samples and Langmuir model fitting results.

(60 mm length, 4 mm inner diameter, 0.2 mm wall thickness) pre-welded at one end, which are then purged with high-purity argon (99.99%) for 2 min to displace residual air before being hermetically sealed under argon protection (Xiao et al., 2005; Gai et al., 2015). The sealed gold tubes are loaded into a stainless steel autoclave reactor (model: HPHT-500) with a 500 mL capacity, which is filled with deionized water as the pressure-transmitting medium. At a confining pressure of 50 MPa (controlled by a precision pressure pump with an accuracy of ± 0.1 MPa), the 10 sub-samples are heated from 50 °C to target temperatures (150, 200, 250, 300, 350, 400, 450, 500, 550, and 600 °C) in a programmable muffle furnace (model: SX2-12-10) with a temperature rise rate of 20 °C/h. The temperature is monitored using a K-type thermocouple inserted into the reactor, with an error of less than ± 1 °C, and the pressure is maintained using an automatic pressure compensation system with an error of less than ± 1 MPa (Tian et al., 2012). After reaching the target temperature, each reactor is rapidly quenched in cold water to terminate the reaction. Post-experiment, the gold tubes are punctured in a vacuum collection system, and gaseous hydrocarbons (C₁–C₁₄) are analyzed using an Agilent 6890N gas chromatograph equipped with a Poraplot Q capillary column (30 m \times 0.25 mm \times 0.25 μ m) and a flame ionization detector (FID), following the method described by Pan et al. (2012). Liquid hydrocarbons (C₁₄₊) are extracted using dichloromethane (CH₂Cl₂) via ultrasonic extraction for 10 min and quantified using gravimetric analysis. Finally, the residual solid samples are subjected to Rock-Eval pyrolysis (model: Rock-Eval 6) and vitrinite reflectance (R_o) measurements using a microphotometer (model: MPV-SP) to determine organic maturity.

Two principal methodologies are conventionally employed for assessing thermal maturity in shale pyrolysis simulation studies: (1) Application of hydrocarbon generation kinetic models, with the most prevalent being the Easy R_o model developed by Sweeney and Burnham (1990); (2) utilization of thermal simulation data from analogous coal samples as maturity proxies for shale specimens, a practice predominantly adopted when vitrinite grains are absent in shale formations (Liu et al., 2022). Given that the investigated samples comprise Type III kerogen-rich shales characterized by elevated organic content and substantial vitrinite

occurrence, R_o measurements are directly employed as the maturity parameter in this investigation.

Rock-Eval pyrolysis can determine the type of organic matter in shale and evaluate the shale's hydrocarbon generation potential, serving as the basis for assessing organic matter diagenesis. According to the T_{max} and Hydrogen Index (HI) cross-plot (Fig. 3(a)), Y23-3 sample is identified as Type III kerogen (Mohamed et al., 2016), with a low HI index not exceeding 127 mg HC/g TOC. T_{max} in the range of 430–465 °C is within the oil generation zone, with a R_o of 1.3%. When T_{max} exceeds 465 °C, the sample enters gas generation zone, with oil generation ability gradually decreasing and gas generation ability increasing. S_1+S_2 represent oil and gas potential of shale (Fig. 3(b)), and when R_o is approximately 2.0%, the slope of curve significantly decreases, indicating that the remaining organic matter's oil and gas generation potential weakens and the rate of oil and gas generation slows.

The analysis results of hydrocarbon products from thermal simulation of ten sub-samples are shown in Fig. 3(c). C₁₋₅ represents gaseous hydrocarbons, C₆₋₁₄ represents light liquid hydrocarbons, and C₁₄₊ represents heavy hydrocarbons. When R_o is approximately 1.2%, large amounts of gaseous hydrocarbons begin to form, primarily generated from the direct degradation of kerogen. When R_o approaches approximately 1.6%, Type III kerogen enters its peak oil generation phase. Notably, the magnitude of oil generation remains significantly lower than concurrent gas production, demonstrating that Type III kerogen exhibits markedly limited oil-generation potential while maintaining robust gas-generating capabilities. This observed threshold ($R_o > 1.6\%$) slightly exceeds the $R_o = 1.5\%$ maturation level documented in the Barnett Shale (United States) (Lewan and Pawlewicz, 2017). Upon reaching R_o values exceeds 2.0%, C₂ undergoes thermal decomposition, marking the onset of dry gas generation. When R_o exceeds 3.0%, near-complete cracking of C₂₊ hydrocarbons occur, accompanied by progressive diminishment of hydrocarbon generation potential, ultimately leading to stabilization of total hydrocarbon yields. The evolutionary pattern demonstrates that Type III kerogen-rich shale systems predominantly yield gaseous hydrocarbons. Beyond the $R_o = 2.0\%$ threshold, methane production persists as the sole increasing component, while subordinate

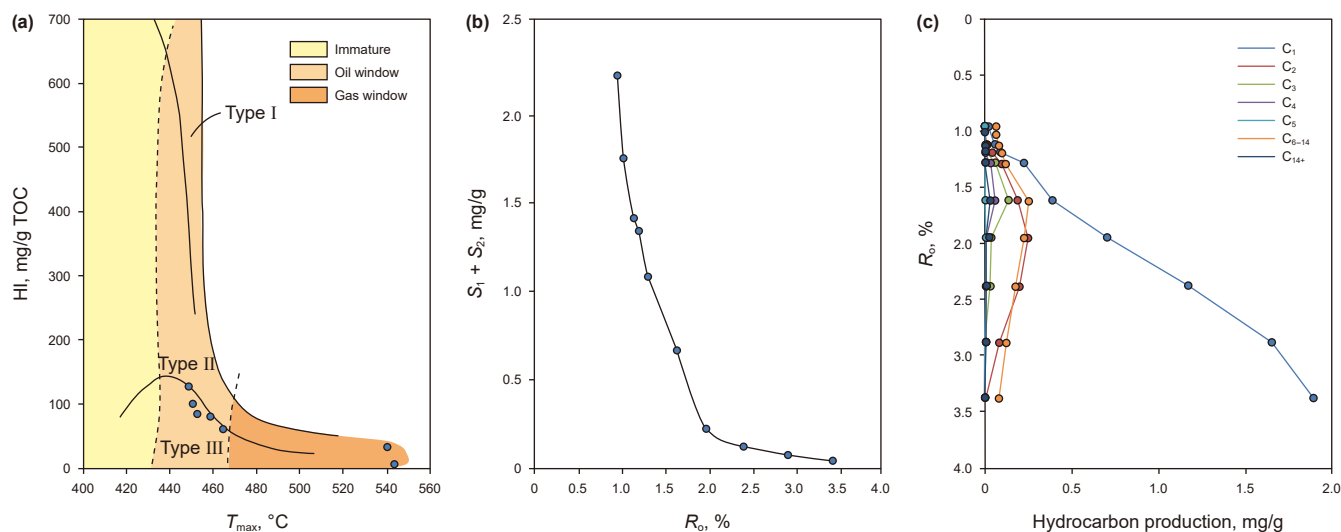


Fig. 3. Thermal simulation and pyrolysis characteristics of sample Y23-3. (a) HI vs. T_{max} cross-plot, illustrating the evolutionary trajectory of organic matter maturity and kerogen type differentiation across progressive thermal simulation stages. (b) S_1+S_2 vs. R_o correlation diagram demonstrating exponential depletion of hydrocarbon generation potential with advancing thermal maturation. (c) Phase-specific hydrocarbon component distribution profiles documenting the dynamic evolution of gaseous and liquid hydrocarbons during pyrolysis.

hydrocarbons experience sequential secondary cracking processes until reaching near-depletion states.

4. Models

Shale gas systems are characterized by self-generation, self-storage, and in-source accumulation (Zhang et al., 2022). The hydrocarbon gases originate from thermal maturation of organic constitutes and become predominantly retained within both organic-hosted nanopores and associated pore networks in adjacent mineral matrices. This inherent geological process results in in situ hydrocarbon generation, storage, and retention within the shale matrix. In this study, models are established from three aspects: kerogen-to-gas transformation kinetics, reservoir space evolution, and occurrence state. These models are coupled with burial process simulations to analyze the shale gas evolution process.

Fig. 4 illustrates the comprehensive technical workflow of this study, which integrates experimental characterization, theoretical modeling, and numerical simulation to reconstruct the gas content evolution in Marine–continental transitional shales (MCTS). The framework begins with multi-temperature methane isothermal adsorption experiments and gold-tube pyrolysis on low-maturity shale samples, providing foundational data on adsorption behavior and hydrocarbon generation kinetics. Subsequently, three core models—hydrocarbon generation, reservoir porosity evolution, and gas occurrence—are developed and calibrated against experimental results. Finally, these models are coupled and applied to simulate gas content evolution under both real and

virtual burial-thermal histories, enabling quantitative analysis of key geological controlling factors.

4.1. Hydrocarbon generation model

Organic matter serves as the fundamental source for hydrocarbon generation, with both its type and content being critical factors determining gas yields. MCTS mainly generate gaseous hydrocarbons, with less oil components (He et al., 2022). Therefore, when establishing the hydrocarbon generation model for Type III organic-rich shales, it is simplified by neglecting the liquid hydrocarbons lost during primary migration, assuming that the organic matter in the shale is entirely the carbon source for shale gas. Additionally, shale gas reservoirs generally exhibit high thermal mature and have entered the gas generation stage. At this stage, the TOC content in the shale represents the residual organic carbon content (TOC_r), which is the amount of organic carbon remaining after a hydrocarbon generation process. To accurately simulate hydrocarbon generation potential and evolution, it is essential to restore the current TOC_r value to their original pre-generation organic carbon content (TOC_o). Integrating these considerations, this study establishes the gaseous hydrocarbon generation model for MCTS as follows:

$$Y = TOC_o \times K \times G \tag{2}$$

In the equation, *Y* is thermal gas yield per unit shale mass, mg/g; TOC_o is original organic carbon content, %; *K* is organic matter type correction factor, dimensionless; *G* is thermal gas generation per unit TOC, mg/g TOC.

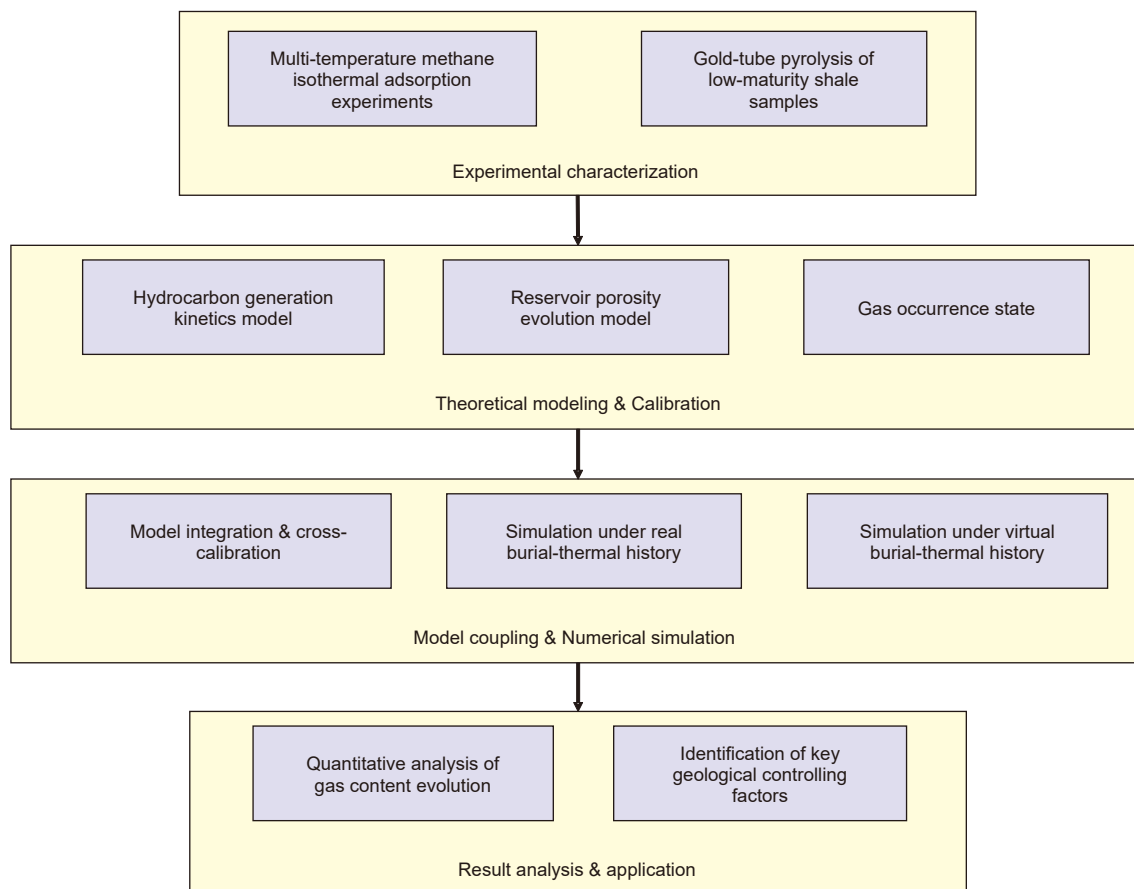


Fig. 4. Comprehensive technical workflow integrating experimentation, modeling, and simulation for analyzing shale gas content evolution in MCTS.

4.1.1. Gaseous hydrocarbon production model

Thermal simulation experiments (Fig. 3(c)) reveal that Type III kerogen exhibits triphasic gas generation behavior with increasing maturity: an initial slow growth phase, followed by rapid acceleration, and ultimately stabilization at maximum yield. The Logistic model equation is $y = 1/(1 + e^{-x})$, whose sigmoidal profile matches organic matter generation patterns (Kudryashov, 2015; Wu and Baleanu, 2014), provides the foundation for our thermogenic gas yield (G) model. By integrating pyrolysis data (gas yield, R_o , and S_2 parameters) from experimental samples, we derive:

$$G = \frac{A}{B + C \times e^{-D \times R_o + E}} \quad (3)$$

where e is natural constant; A to E are constants.

Nonlinear regression analysis using the least squares method yields the calibrated Eq. (4) with a determination coefficient (R^2) of 0.979. The derived model effectively captures three characteristic phases of gas generation: (1) initial slow accumulation (immature stage), (2) rapid gas escalation (peak generation window), and (3) ultimate production plateau (post-maturity phase). This triphasic behavior closely aligns with theoretical hydrocarbon generation mechanisms, as visually demonstrated in Fig. 5(a).

$$G = \frac{4.788}{0.0399 + 0.260 \times e^{-2.796 \times R_o + 3.404}} \quad (4)$$

4.1.2. Kerogen correction factor (K)

Hydrogen-to-carbon (H/C) ratio, oxygen-to-carbon (O/C) ratio, and kerogen functional groups collectively govern kerogen's hydrocarbon generation capacity. Significant heterogeneity exists among Type III kerogen derived from distinct depositional settings and precursor materials. Within Rock-Eval pyrolysis experiments, S_2 represents the hydrocarbons generated from organic matter pyrolysis, which has a significant impact on the thermal evolution of gaseous hydrocarbons and is also an important indicator of the rock's hydrocarbon generation potential (Hakimi et al., 2010; Peters, 1986; Varma et al., 2018). Progressive thermal maturation (increasing R_o) promotes organic carbon conversion to mobile gaseous hydrocarbons, resulting in systematic S_2 depletion in residual samples (Fig. 5(b)). To reflect the differences in hydrocarbon generation potential between different shale samples, the kerogen correction factor (K) is introduced. Here, the thermal simulation residue of the Y23-3 sample is used as the standard, with its pyrolysis S_2 value serving as the reference baseline. The kerogen

correction factor for the Y23-3 sample is defined as $K = 1$. The relationship between S_2 , K , and R_o also follows the Logistic model:

$$S_2 = K \times \frac{A}{B + C \times e^{-D \times R_o + E}} \quad (5)$$

In the equation, S_2 is pyrolytic hydrocarbon yield per unit TOC mass in the 300–600 °C range, mg/g TOC; K is kerogen correction factor, with the Y23-3 sample set to 1.

The fitting results are shown in Eq. (6), with an R^2 of 0.994 (Fig. 5(b)):

$$S_2 = K \times \frac{-5.296}{-0.0328 - 0.0189 \times e^{3.241 \times R_o - 3.224}} \quad (6)$$

Eq. (6) can be rearranged as:

$$K = S_2 \times \frac{0.0328 + 0.0189 \times e^{3.241 \times R_o - 3.224}}{5.296} \quad (7)$$

Using Eq. (7), K can be calculated for any Type III kerogen shale sample using S_2 and R_o , which can be used to correct for differences in hydrocarbon generation potential between any sample and the Y23-3 sample.

4.1.3. Organic carbon recovery coefficient (r)

The organic carbon recovery coefficient (r) is defined as the ratio of TOC_o to TOC_r :

$$r = TOC_o / TOC_r \quad (8)$$

The hydrocarbon generation potential (HGP) method is a classic approach in petroleum system analysis for restoring original organic carbon. Its theoretical basis lies in the principle of material balance, which means that the organic matter in the source rock maintains constant mass before and after hydrocarbon generation (Pang et al., 2005). Organic carbon is considered to consist of two parts: effective carbon and ineffective carbon. Ineffective carbon remains inert throughout thermal maturation, whereas effective carbon converts to hydrocarbons that are subsequently expelled. The r is calculated based on the hydrocarbon generation potential index ($GPI = (S_1 + S_2)/TOC$) as follows:

$$r = \frac{1 - 0.83 \times GPI_r / 1000}{1 - 0.83 \times GPI_o / 1000} \quad (9)$$

where the constant (0.83) is effective carbon recovery coefficient; GPI_r is current hydrocarbon generation potential index at a certain maturity, mg/g TOC; GPI_o is original hydrocarbon generation

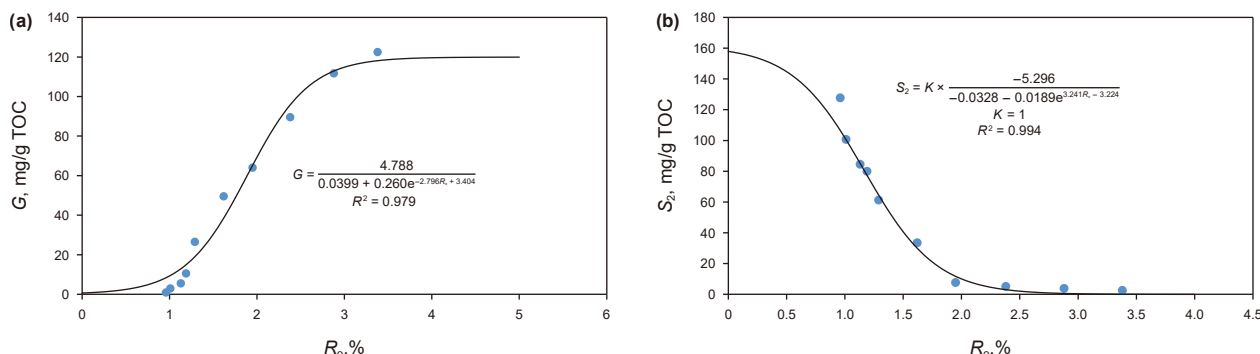


Fig. 5. (a) Fitting results of the gaseous hydrocarbon production model. (b) The relationship between S_2 and R_o .

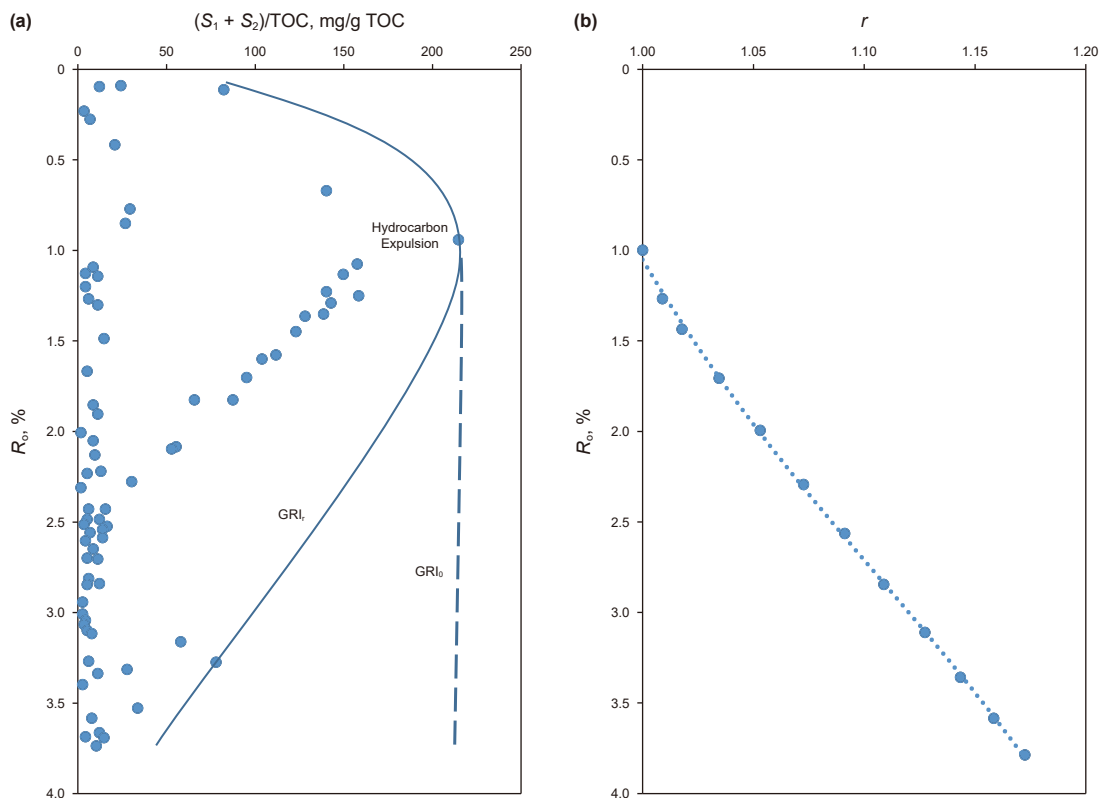


Fig. 6. (a) Application of hydrocarbon generation potential theoretical model in MCTS; (b) type III Kerogen organic carbon recovery coefficient.

potential index, corresponding to the R_0 threshold for expulsion, mg/g TOC.

Fig. 6(a) presents the implementation of the hydrocarbon generation potential model on Rock-Eval pyrolysis data from MCTS, while Fig. 6(b) demonstrates calculated r for these systems. Analytical results reveal comparatively lower r -values (≤ 1.2 at $R_0 = 4.0\%$) in Type III kerogen-dominated MCTS, exhibiting significantly reduced carbon restoration capacity relative to their Type I/II counterparts. The fitting results for r are as follows:

$$\begin{cases} r = 1, 0 < R_0 \leq 1 \\ r = 0.0049 \times (R_0 - 1)^2 + 0.049 \times R_0 + 1, R_0 > 1 \end{cases} \quad (10)$$

Combining Eqs. (8) and (10), the formula for calculating the TOC_0 is:

$$\begin{cases} TOC_0 = TOC_r, 0 < R_0 \leq 1 \\ TOC_0 = TOC_r \times (0.0049 \times (R_0 - 1)^2 + 0.049 \times R_0 + 1), R_0 > 1 \end{cases} \quad (11)$$

4.2. Reservoir space evolution model

The investigation of shale porosity evolution originated from early petrophysical studies stemming from analyses of mudstone compaction and pore water expulsion. The widely recognized and applied model in petroleum geology is Athy's effective stress-porosity model (Athy, 1930). Under hydrostatic conditions where

effective stress exhibits linear correlation with burial depth, the porosity-depth profile follows an exponential decay function:

$$\varphi = \varphi_0 \times e^{-k \times Z} \quad (12)$$

φ is mudstone porosity, %; φ_0 is initial porosity of fine-grained sediments, %; Z is burial depth, m; e is natural constant, approximately 2.718; k is coefficient, related to the rock's physical properties.

While Athy model provides a foundational framework, its oversimplified nature fails to capture lithology-specific porosity evolution in shales with varying mineralogical compositions, grain size distributions, and burial histories (Fig. 7(a)). Advanced petrographic analyses reveal that organic-rich shale reservoirs predominantly contain organ porosity and hydrocarbon-induced shrinkage fractures rather than intergranular mineral pores, particularly in thermally mature systems hosting commercial gas accumulations (Chalmers et al., 2012). Therefore, the reservoir space evolution of shale during burial is influenced not only by mechanical compaction and other physical diagenetic processes but also by organic matter thermal evolution and clay mineral transformation during thermal diagenesis (Liu et al., 2024).

Our previous work (Yang and Guo, 2020) established a process-responsive model for MCTS through differential formalism:

$$d\varphi(Z, R_0) = f(\omega_k, \omega_o) dZ \quad (13)$$

R_0 is average vitrinite reflectance measured in thermal simulation experiments, %; ω_k is percentage of kaolinite, %; ω_o is percentage of other clay minerals, %.

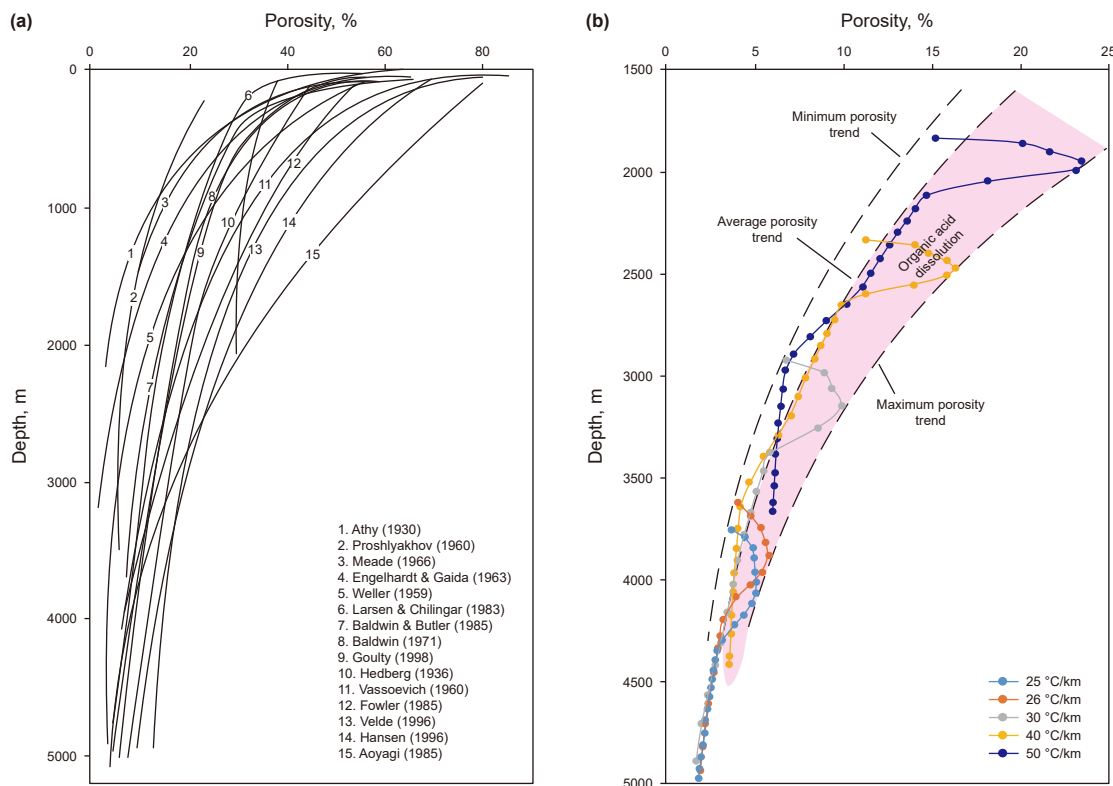


Fig. 7. (a) Evolutionary curves of mudstone porosity in different basins and formations. (b) Evolution process of multi-parameter porosity model for R_0 above 1.0% (modified by Mondol et al., 2007; Yang and Guo, 2020).

This integrated model incorporates multiple controlling factors (clay mineralogy, burial depth, and thermal maturity) through differential analysis to characterize progressive changes in petrophysical properties during maturation. It enables systematic computation of porosity evolution trajectories for shales with varying compositional assemblages and maturation histories (Fig. 7(b)). This model also considers the effects of organic acid-mediated dissolution, illitization of clay minerals, and hydrocarbon-induced organic porosity development, making it suitable for the quantitative calculation of pore space in high-maturity shale gas reservoirs (Yang and Guo, 2020).

4.3. Methane occurrence model

Methane exhibits preferential solubility in petroleum phases compared to aqueous systems. Therefore, the dissolved gas content in Type III shale is negligible. Subsurface analyses demonstrate dissolved methane concentrations in formation waters typically constitute < 3% of adsorbed gas inventories (Curtis et al., 2012). Consequently, this study focuses exclusively on adsorbed and free gas phases.

4.3.1. Adsorbed gas model

Within the Langmuir absolute adsorption model, systematic correlations exist between Langmuir volume (V_L) and key geological parameters (Fig. 8(a) and (b)). Robust inverse correlations emerge between V_L and formation temperature ($R^2 = 0.9854$), while positive linear relationships V_L -TOC associations ($R^2 = 0.8508$). Mineralogical constituents, including quartz and clay percentages, demonstrate statistically insignificant relationships with adsorption parameters.

An empirical relationship between temperature, TOC, and V_L is established. Constrained by physical principles, V_L must maintain positive values while exhibiting temperature-dependent attenuation. An exponential function is used as the main function to establish the fitting formula. The TOC content affects the adsorption capacity but does not influence the trend, so it is used as the coefficient in the main function. The specific formula is as follows:

$$V_L = (a \times \text{TOC} + b) \times e^{-c \times T} \tag{14}$$

V_L is Langmuir volume of shale sample, cm^3/g ; T is temperature, $^\circ\text{C}$; a , b , and c are fitting coefficients.

Multivariate nonlinear regression analysis yields calibrated coefficients ($a = 0.3718$, $b = 2.0386$, $c = 0.0073$) with a composite determination coefficient ($R^2 = 0.919$), confirming robust predictive capability. This formulation strictly maintains $V_L > 0$ across thermal maturation spectra, demonstrating operational validity even under extreme burial conditions (>3,500 m depth) where elevated geothermal gradients prevail (Fig. 9(a)).

The established empirical formulation governing V_L -TOC-temperature relationships is expressed as:

$$V_L = (0.3718 \times \text{TOC} + 2.0386) \times e^{-0.0073 \times T} \tag{15}$$

There is a strong linear correlation between Langmuir pressure (P_L) and temperature in Fig. 8(c). Thermodynamically, this relationship derives from adsorption enthalpy (ΔH) and entropy (ΔS^0) through the Clausius-Clapeyron equation (Myers and Monson, 2002):

$$\ln P_L = \frac{\Delta H}{R(T + 273.15)} - \frac{\Delta S^0}{R} + \ln p^0 \tag{16}$$

ΔH is adsorption enthalpy, which is equal to the adsorption

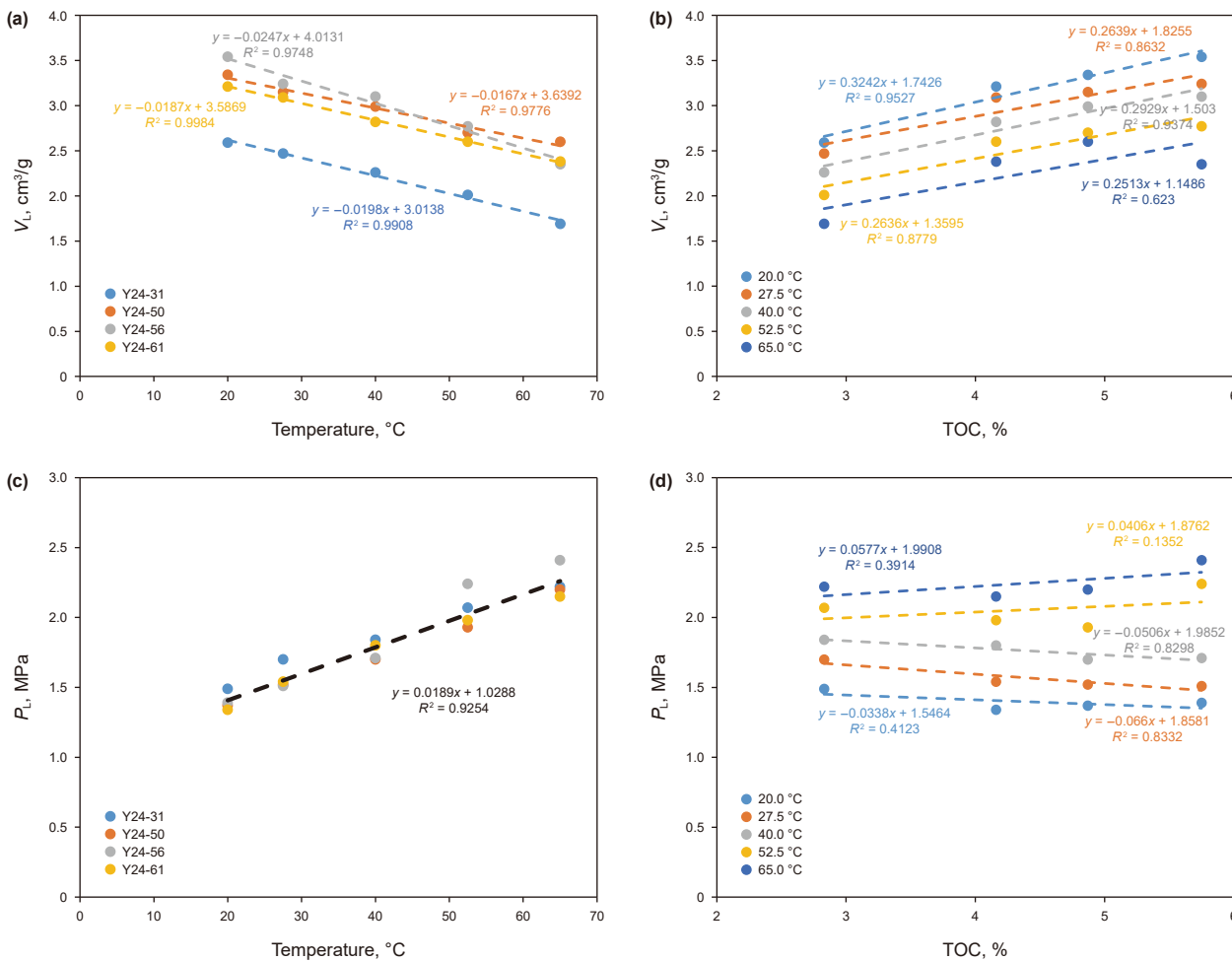


Fig. 8. The relationships between Langmuir parameters and T, TOC.

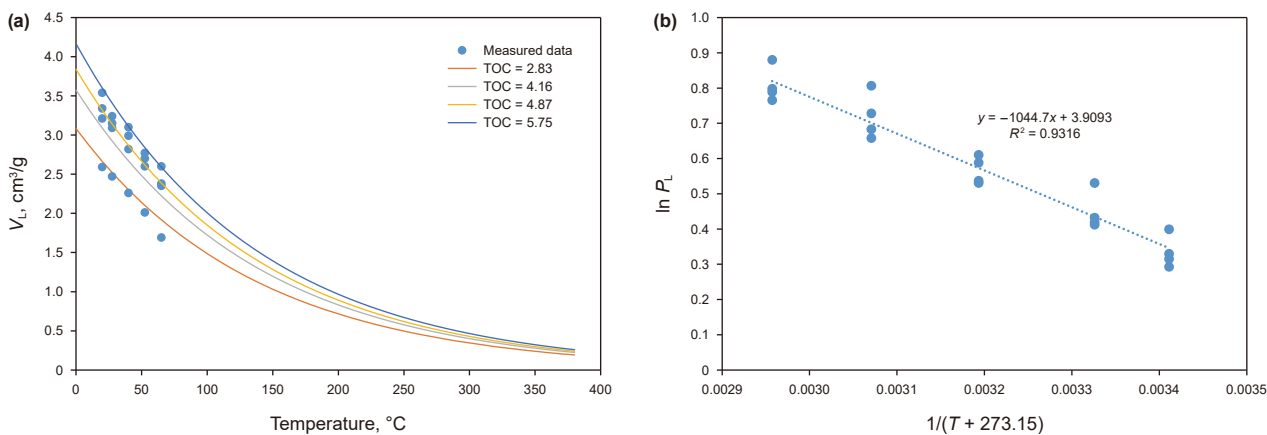


Fig. 9. (a) Measured data and fitting effect of V_L at different TOC. (b) Fitting relationship between P_L and T using the Clausius-Clapeyron equation.

heat, kJ/mol; Δs^0 is standard adsorption entropy, $J \cdot mol^{-1} K^{-1}$; R is ideal gas constant, $8.3145 J \cdot mol^{-1} K^{-1}$; p^0 is standard pressure, 0.101 MPa; T is temperature, $^{\circ}C$.

Regression analysis yields the temperature-dependent P_L relationship ($R^2 = 0.962$, Fig. 9(b)):

$$\ln P_L = \frac{-1044.7}{T + 273.15} + 3.9093 \tag{17}$$

Combining Eqs. (16) and (17) with the Langmuir equation, adsorbed gas (V) becomes:

$$V = \frac{P \times (0.3718 \times \text{TOC} + 2.0386) \times e^{-0.0073 \times T}}{P + e^{\frac{-1044.7}{T+273.15} + 3.9093}} \quad (18)$$

V is adsorbed gas per unit shale mass at standard conditions, cm^3/g ; P is pressure, MPa.

4.3.2. Free gas model

Free gas refers to unbound hydrocarbons occupying interconnected pore networks and fracture systems. Given the unpredictable density variations in mixed hydrocarbon gases under changing thermobaric conditions and compositional gradients, coupled with pyrolysis evidence demonstrating methane dominance (>98% vol.) in Type III kerogen-derived gases at high maturity stages ($R_o > 2.0\%$), we adopt methane as the representative free gas component. Crucially, adsorbed-phase methane occupies measurable pore volume (Law et al., 2003), necessitating storage space correction through:

$$V_{\text{free}} = V_p - V_{\text{ads}} \quad (19)$$

V_{free} is maximum free gas storage capacity, cm^3/g , in-situ conditions; V_p is total accessible porosity, cm^3/g ; V_{ads} is adsorbed gas volume under formation conditions, cm^3/g .

The relationship between pore volume and porosity is given by:

$$V_p = \frac{\varphi}{100 \times \rho_{\text{rock}}} \quad (20)$$

φ is subsurface shale porosity from multi-porosity modeling, %; ρ_{rock} is bulk density of in-situ shale, g/cm^3 .

The adsorbed gas volume can be expressed as:

$$V_{\text{ads}} = V_{\text{ads}_s} \times \frac{\rho_{\text{std}}}{\rho_{\text{ads}}} \quad (21)$$

V_{ads_s} is adsorbed methane volume per unit mass of shale at standard conditions, cm^3/g ; ρ_{std} is methane density at standard conditions, $0.716 \times 10^{-3} \text{ g}/\text{cm}^3$; ρ_{ads} is density of adsorbed methane, g/cm^3 . It is generally assumed that the density of adsorbed methane does not exceed $0.424 \text{ g}/\text{cm}^3$ (liquid methane density at 0.1 MPa boiling point) or $0.373 \text{ g}/\text{cm}^3$ (van der Waals volume estimation (Gasparik et al., 2013)).

Methane reaches supercritical state ($T_{\text{critical}} = -82.59 \text{ }^\circ\text{C}$, $P_{\text{critical}} = 4.59 \text{ MPa}$ (Zhang et al., 2021)) at depths > 500 m where conventional PVT equation become invalid. High-precision methane density calculations in the supercritical state are based on the

equation of state proposed by Setzmann (Setzmann and Wagner, 1991), with NIST providing implementation parameters (Fig. 10).

The volume of free methane at standard conditions can be expressed as:

$$V_{\text{free}_s} = V_{\text{free}} \times \frac{\rho_{\text{NIST}}}{\rho_{\text{std}}} \quad (22)$$

V_{free_s} is maximum free gas content at standard conditions, cm^3/g ; ρ_{NIST} is NIST-derived methane density under in-situ reservoir conditions.

By integrating Eqs. (20) and (21) the formation-condition free gas capacity is derived as:

$$V_{\text{free}_s} = \left(\frac{\varphi}{100 \times \rho_{\text{rock}}} - V_{\text{ads}_s} \times \frac{\rho_{\text{std}}}{\rho_{\text{ads}}} \right) \times \frac{\rho_{\text{NIST}}}{\rho_{\text{std}}} \quad (23)$$

5. Discussion

5.1. Gas content evolution in the Shanxi Formation, Southern North China Basin

Y22 Well in the Southern North China Basin was selected as a typical well to simulate the evolution of shale gas content using our integrated models. These models simulated dynamic variations in adsorbed gas, free gas, and total gas content throughout geological history. The Permian Shanxi Formation in Y22 Well exhibits complex process of subsidence and uplift, and currently resides at high thermal maturity ($R_o = 3.2\%$), which allows for a good reflection of the shale gas generation and occurrence state evolution during organic maturation.

5.1.1. Burial-thermal history

The Basin underwent rapid crustal thinning under Permian–Triassic (284–200 Ma) extensional tectonics (Tang et al., 2018), accompanied by progressive increases in paleo-heat flow ($90 \rightarrow 110 \text{ mW}/\text{m}^2$) and geothermal gradients ($35 \rightarrow 45 \text{ }^\circ\text{C}/\text{km}$). Subsequent Yanshanian–Himalayan compression induced structural differentiation, with intense uplift (>2 km denudation) in the Taikang Uplift sector. This tectonic phase coincided with peak hydrothermal activity (180–120 Ma), evidenced by widespread volcanoclastic deposits and calibrated thermal indicators. Using PetroMod software, the burial and thermal history (by Easy R_o model) of the Shanxi Formation in Well Y22 of the Taikang Uplift was reconstructed and calibrated with current measured R_o data (Fig. 11).

Factors and explanations not considered in the simulation process: (1) Unaccounted for overpressure: undercompaction, hydrocarbon generation, and poor fluid expulsion often lead to overpressure during burial, but paleopressure quantification remains elusive, and this study lacks relevant data support. Furthermore, due to multistage Cenozoic uplift events and adjustments, the Shanxi Formation shale is currently at hydrostatic conditions, so overpressure is not considered in this study. (2) Unaccounted for formation water occupying adsorption sites: in fact, the water saturation significantly affects shale adsorption capacity. When there is a small amount of water, the shale's adsorption capacity rapidly decreases (Ma and Yu, 2020), and formation water also occupies pore space, affecting free gas content. However, since it is difficult to predict the formation water saturation during geological history, this study simulates the "maximum" gas content under the assumption of no water, which reflects the shale reservoir's maximum gas storage capacity (Hao

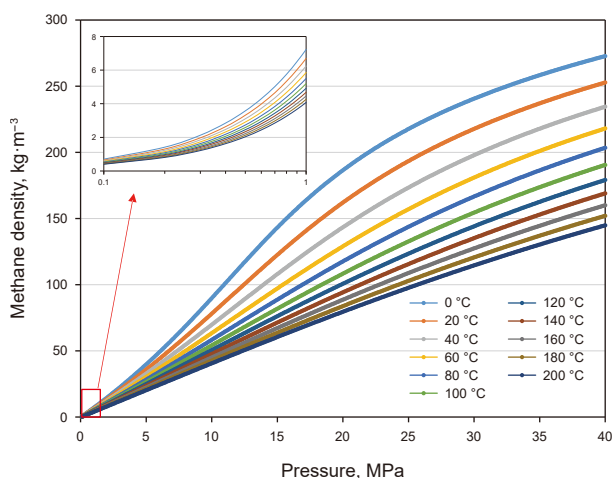


Fig. 10. Dependence of supercritical methane density on thermobaric conditions.

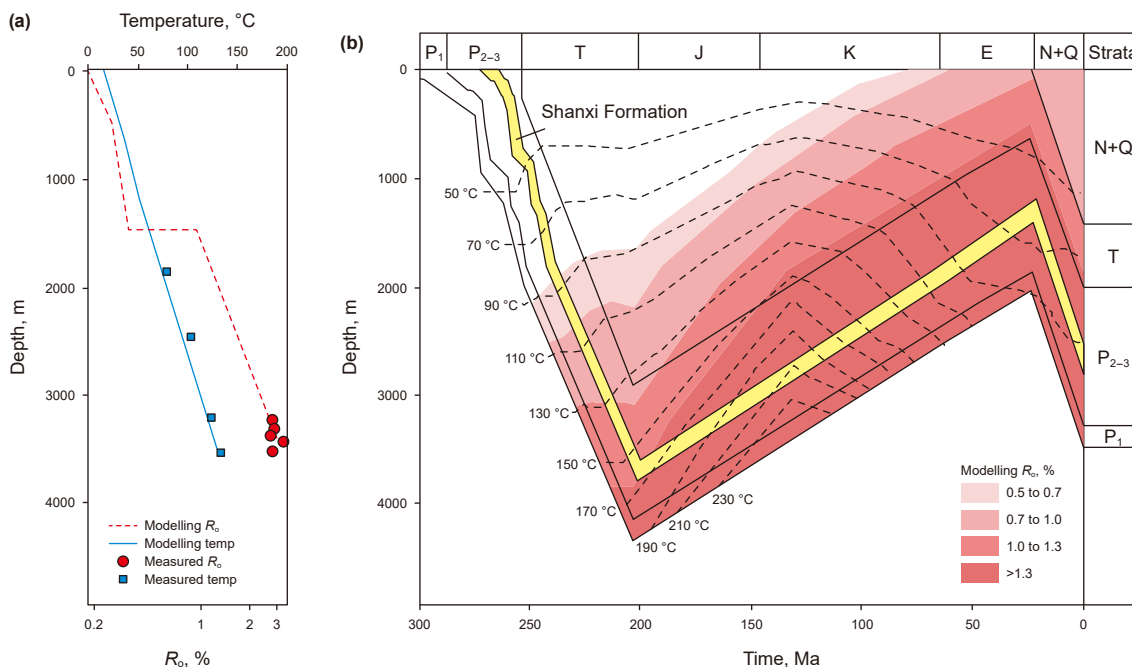


Fig. 11. Burial and thermal history of well WC1 of Shanxi Formation. The “temp” in the legend denotes temperature.

et al., 2013). The actual gas content should be lower than this value.

5.1.2. Evolution stages and characteristics

The MCTS reservoir of the Shanxi Formation in Y22 Well has a current TOC content of 2.4%, a vitrinite reflectance of 3.2%, and burial depth of 2732.5 m. As illustrated in Fig. 12, the evolutionary process can be roughly divided into seven distinct phases (Stages A–G):

Stage A: During this phase, the strata undergo rapid subsidence to approximately 1500 m burial depth. Thermally immature organics ($R_o < 0.4\%$) show negligible thermogenic gas generation, while potential biogenic methane production (excluded from this analysis) may occur (Park and Liang, 2016). Characterized by mechanical compaction of unconsolidated fine-grained sediments, this stage features intense porosity reduction (53%→20%) driven by interstitial water expulsion through developing permeability pathways.

Stage B: Sustained burial elevates formation temperature (>70 °C) and pressure, driving organic maturation ($R_o = 0.4\%–1.3\%$). Kerogen-derived organic acids have a corrosive effect on minerals such as K-feldspar in the shale, which significantly increases porosity and forms dissolution windows (Ma et al., 2022). The main feature of this stage is that as gaseous hydrocarbons continue to increase, natural gas is adsorbed onto the surfaces of organic matter and clay minerals. Due to the increase in temperature, the maximum adsorbed gas volume decreases. By the end of this stage, the total gas generation volume is sufficient to meet the shale’s adsorbed gas capacity.

Stage C: At burial depths exceeding 3000 m ($EasyR_o > 1.3\%$), hydrocarbon generation peaks through thermal cracking of kerogen and early-formed hydrocarbons. Methane-dominated gas migrates into pore networks, predominantly occupying free-phase states. Elevated thermobaric conditions reduce maximum adsorption capacity (refers to the maximum amount of natural gas that a unit mass of shale can adsorb under specific temperature and pressure conditions when saturation is reached) by 40%–45%, triggering partial desorption and phase transition to free gas.

Supercritical methane (density > 128 g/L, 178×STP methane density) achieves exceptional storage efficiency under these conditions. By the end of this stage, shale porosity has decreased to 3.5%, and both adsorbed gas and free gas content have reached saturation, at 0.67 and 2.21 cm³/g, respectively.

Stage D: Progressive burial reaches maximum depths (3,700 m) with thermal maturation exceeding $EasyR_o > 2.0\%$, transitioning organic matter into the overmature phase. Type III kerogen still has some gas generation potential in the overmature stage, the organic matter continues to generate gas. This stage corresponds to the late diagenetic B period, during which clay minerals evolve into regular and dense illite and illite-smectite mixed layers (Wang et al., 2023). As the overlying pressure and effective stress continue to increase, porosity gradually decreases to its minimum value. During this process, both the maximum free gas and maximum adsorbed gas volumes decrease. These gases, along with newly generated gaseous hydrocarbons, are expelled into adjacent sandstone reservoirs or shallow layers. This expulsion drives a rapid increase in expelled gas volume until it peaks.

Stage E: Tectonic reversal occurs, and the strata are compressed and uplifted. Organic maturation continues at decelerated rates ($EasyR_o$ still increasing), generating a small number of hydrocarbons. Tectonic activity and depressurization improve the shale reservoir to some extent, slightly increasing porosity and the maximum free gas volume. The decrease in temperature also slightly increases the maximum adsorbed gas volume. A small amount of hydrocarbons generated during this stage partially replenishes the adsorbed gas, while the remaining portion enters the pores and replenishes the free gas volume, causing the in-situ gas content to rise correspondingly.

Stage F: The strata continue to experience significant uplift, halting thermal evolution and hydrocarbon generation. The in-situ gas content peaks at 1.94 cm³/g. As temperatures drop markedly, the maximum adsorbed gas volume increases considerably. The primary characteristic of this stage is the conversion of free methane into adsorbed methane within the pores. Around 100 million years, the free gas volume and adsorbed gas volume reach their values simultaneously, each at 0.97 cm³/g.

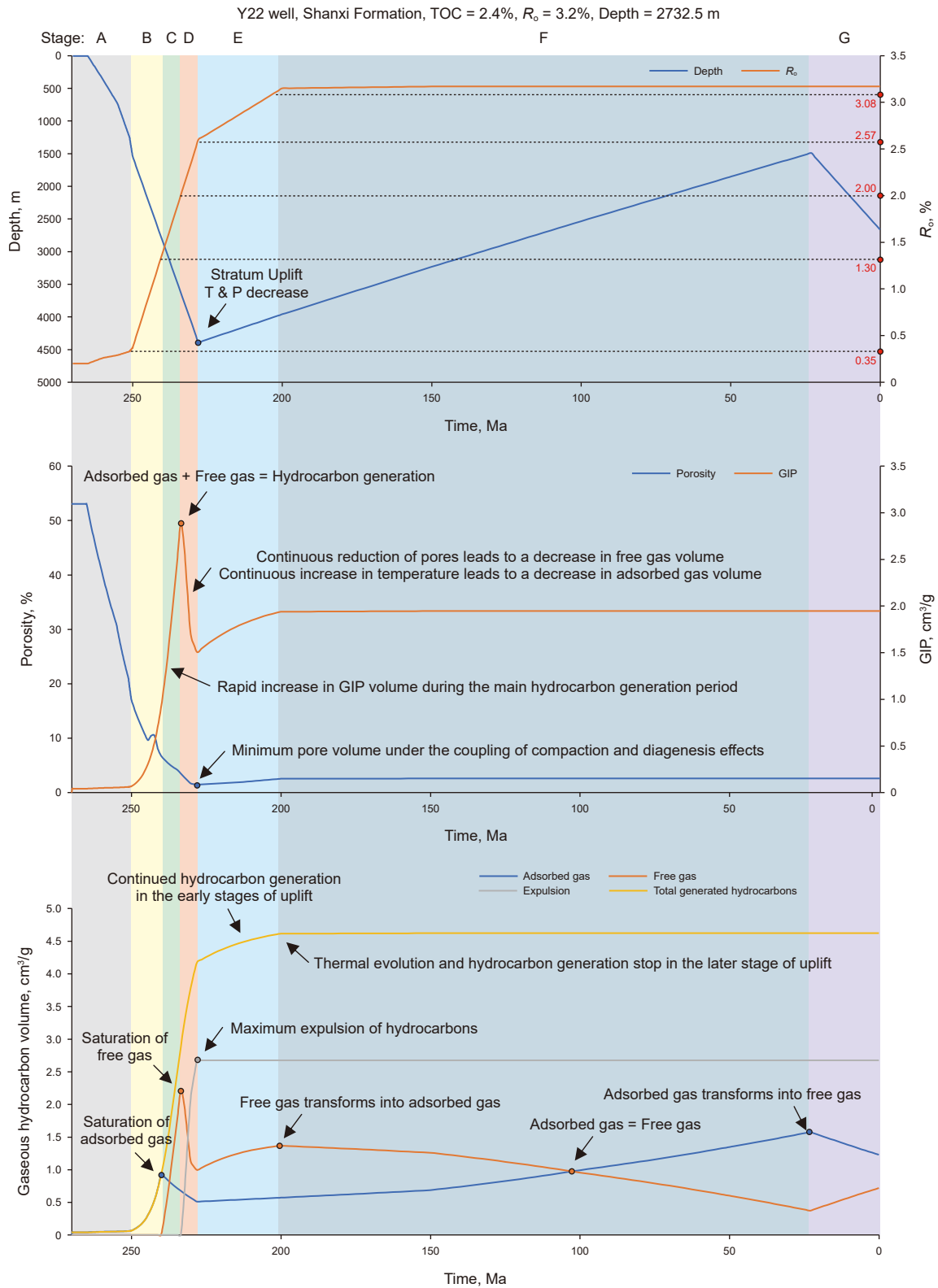


Fig. 12. Displays the evolutionary simulation results of shale gas content in Well WC1 of the Shanxi Formation. The thermal maturity model is based on the Easy R_o model from the PetroMod 1D basin modeling software. The porosity model incorporates Yang et al.'s approach, accounting for shale thermal processes and clay mineral content (Yang and Guo, 2020). Gas expulsion from the shale occurs once hydrocarbon generation surpasses the maximum storage capacity, which includes both free gas and adsorbed gas.

Table 3
Statistical table of simulation parameters for various virtual burial processes.

ID	TOC, %	Maximum burial depth, m	Uplift amplitude, m	Paleo-heat flow, mW/m ²	Pressure coefficient	R _o , %	Remarks
T1	0.5	4371	2881	/	1.0 (Normal pressure)	3.2	The burial and thermal history are consistent with Well Y22.
T2	1						
T3	1.5						
T4	2						
T5	3						
T6	4						
T7	6						
T8	8						
T9	10						
D1	3	2500	1000	65		1.15	
D2		3000				1.58	
D3		3500				2.18	
D4		4000				2.84	
D5		4500				3.55	
U1	3	4000	0	65		3.19	/
U2			500			2.83	
U3			1000			2.66	
U4			2000			2.44	
H1	3	4000	2000	50		1.46	/
H2				55		1.76	
H3				60		2.1	
H4				65		2.44	
H5				70		2.83	
H6				75		3.23	
P1	3	4000	0	65	1.0	3.19	Overpressure occurs when EasyR _o = 1.2%; the overpressure reaches its maximum when EasyR _o = 2.0%.
P2					1.1		
P3					1.2		
P4					1.3		

Stage G: The strata undergo secondary burial, yet the burial depth remains below the historical maximum burial depth, causing thermal evolution to cease. However, temperature and pressure continue to rise, including a decrease adsorbed gas and its transformation into free gas.

5.2. Controlling factors of shale gas content evolution

The factors influencing in-situ gas content are intricate and multifaceted. The natural gas currently retained present in shale reservoirs results from the combined effects of initial depositional conditions (Chen et al., 2023), reservoir evolution (Jin and Nie, 2022), burial processes (Tang et al., 2021), thermal processes (Guo et al., 2023) and pressure evolution (Li et al., 2023). To gain a better understand of how each individual factors impacts the in-situ gas content in shale, virtual burial and thermal histories have been established. Furthermore, by combining shale evolution models with a control variable approach, this study delves into the dominant controlling factors that control in-situ gas content in shale. Simulation parameters are presented in Table 3, and the simulation results are illustrated in Fig. 13.

5.2.1. TOC

TOC is a key factor in evaluating shale gas as it affects both hydrocarbon generation and the adsorption capacity of shale (Pan et al., 2020). By vary the TOC content while holding burial and thermal histories constant, the shale's gas content evolution can be compared (Table 3). The results show (Fig. 13) that a positive correlation between TOC and in-situ gas retention. Adsorbed gas content is most affected by TOC, especially after uplift, where adsorbed gas content is significantly influenced by TOC. Once TOC exceeds 2%, free gas can fill the pores, and its content becomes less dependent on TOC and more on pore volum e. As TOC increases, hydrocarbon generation also increases, and the reservoir reaches

hydrocarbon saturation and expulsion earlier. Thus, in specific burial processes, especially when the focus is on shallow shale gas reservoirs (depths < 2000 m), adsorbed gas should be the primary consideration, with TOC content being a crucial factor in evaluation.

5.2.2. Maximum burial depth

The burial process significantly impacts the temperature, pressure, and duration of shale's geological history (Fu et al., 2023), thereby affecting thermal maturation, hydrocarbon generation, and reservoir evolution. To investigate the influence of maximum burial depths on shale for gas occurrence, different maximum burial depths were simulated under similar burial processes (Table 3). The results reveal (Fig. 13) that maximum burial depth considerably affects maturity. For five virtual samples with maximum burial depths from 2500 to 4500 m, maturity ranges from 1.2% to 3.6%, spanning various gas generation stages. Greater burial depths lead to higher maturity and enhanced gas generation. However, maximum burial depth also significantly affects shale porosity. Deeper burial cause earlier onset of acidification and porosity enhancement, resulting in a denser reservoir (Li et al., 2016). Thus, there is a trade-off between hydrocarbon generation and reservoir space. An optimal maximum burial depth can enhance shale gas enrichment. Under a paleo-heat flow of 65 mW/m², the results show that samples D1 and D2 with shallower burial depths, exhibit low maturity and limited hydrocarbon generation, failing to reach the shale's maximum gas storage capacity. In contrast, samples D4 and D5, which experienced deeper burial, underwent strong diagenesis with significant compaction and early-stage dissolution. While they generated substantial gas, most of it was expelled. Sample D3, with the highest current in-situ gas content, had a maximum burial depth of 3500 m and a current EasyR_o of 2.2%. This suggests that the combined effects of burial depth and thermal history on gas content are complex and

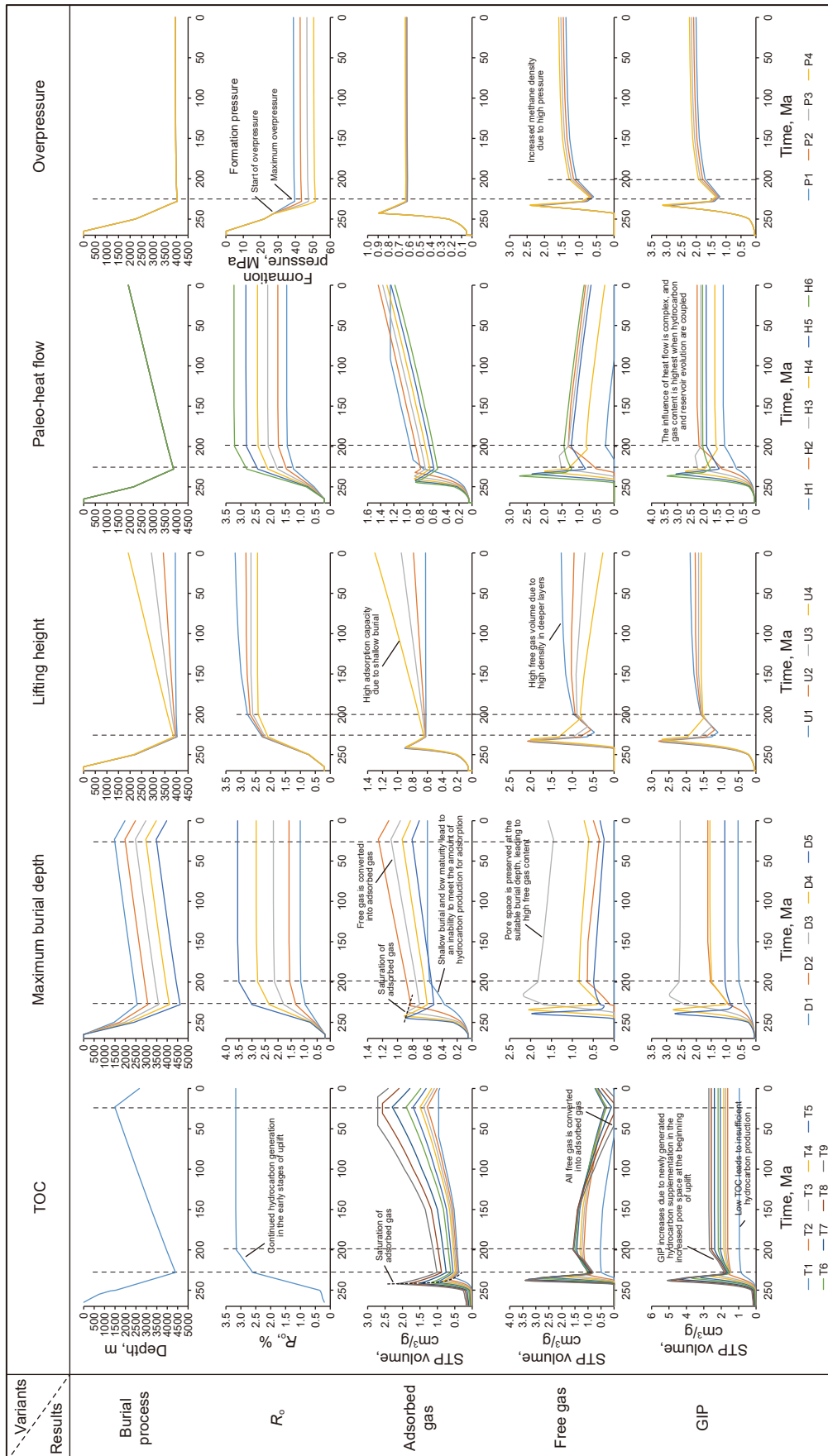


Fig. 13. Evolutionary simulation results of gas content under various virtual burial conditions.

require case-specific analysis under different thermal histories and TOC conditions.

5.2.3. Uplift amplitude

In China, since the Triassic period, sedimentary strata have generally undergone uplift and erosion, with varying degrees of uplift across different regions. During uplift, the decrease in temperature and pressure leads to the cessation of organic matter thermal maturation and also affects the density of free gas and the adsorption capacity of shale (Miao et al., 2023). By maintaining a constant thermal history and TOC content while varying uplift amplitudes (0–2000 m) for burial processes (Table 3), the impact of uplift amplitude on in-situ gas content can be explored. The results show (Fig. 13) that under the same maximum burial depth but different uplift amplitudes, the thermal maturity of shale varies. When the uplift amplitude is 0 m or 500 m, maturity still increases slowly. After an uplift amplitude of 1000 m, the thermal maturation ceases. Uplift causes free gas to transform into adsorbed gas, with some free gas being expelled. This occurs because the reduction in temperature and pressure lowers the density of free gas, causing it to expand and exceed the pore volume of the reservoir. Overall, the total gas content decreases with increasing uplift amplitude. Sustained burial and late-stage uplift are more favorable for shale gas enrichment compared to early-stage uplift.

5.2.4. Geothermal gradient

Geothermal temperature, paleo-heat flow, and thermal events are the primary controls on shale maturity, which in turn affects the history of hydrocarbon generation and diagenetic evolution. By setting different paleo-heat flow values (50–75 mW/m²), the impact of thermal history on shale gas content can be discussed (Table 3). The results indicate (Fig. 13) that paleo-heat flow has a complex effect on gas content. Very high heat flow causes organic matter to mature and generate hydrocarbons rapidly, with intense diagenesis. This leads to the expulsion of a large amount of gaseous hydrocarbons before the maximum burial depth is reached, preventing the full retention of natural gas within the shale. On the other hand, very low heat flow inhibits the complete maturation of organic matter, resulting in insufficient hydrocarbon generation to fill the shale's storage capacity. Under this burial process, a paleo-heat flow of 55–60 mW/m² yields the maximum in-situ gas content.

5.2.5. Overpressure

Successful shale gas fields in China, such as the Fuling and Jiaoshiba fields in the Sichuan Basin, exhibit overpressure characteristics. By setting different hydrocarbon-expulsion pressure gradients (Table 3), this study explores the impact of overpressure on shale reservoir storage capacity. The results show (Fig. 13) that overpressure mainly influences free gas content, as the density of supercritical methane increases with pressure. At high temperatures, pressure has a weak effect on adsorbed gas, and the shale's adsorption capacity also decreases at elevated temperatures. It should be noted that this model does not consider the overpressure and reservoir transformation caused by tectonic compression. In reality, overpressured reservoirs are more significant for reflecting the reservoir's sealing and preservation conditions (Hao et al., 2013; Jin and Nie, 2022). Therefore, overpressure has a greater impact on shale gas enrichment than suggested by this simulation.

6. Conclusion

Based on experiments such as methane isothermal adsorption and gold-tube pyrolysis under formation conditions, an integrated

model for hydrocarbon generation, reservoir space evolution, and natural gas occurrence in MCTS has been established. The Shanxi Formation shale in the Southern North China Basin exhibits a seven-stage (A–G) evolution pattern. Critical thresholds include: dissolution-enhanced reservoir modification at EasyR₀ = 1.0%; adsorbed gas saturation at EasyR₀ = 1.3%; dual saturation of free and adsorbed gas at EasyR₀ = 2.0%; and free-to-adsorbed gas conversion during tectonic uplift.

The evolution of gas content in transitional shales is subject to complex control by multiple factors. TOC shows a significant positive correlation with gas content, particularly influencing adsorbed gas storage capacity in the post-uplift period. Maximum burial depth and paleo-heat flow exhibit complex nonlinear effects. Tectonic uplift magnitude negatively impacts total gas content by reducing pressure/temperature and inducing gas phase transitions. Overpressure enhances free gas storage through increased supercritical methane density.

This study reveals the coupled evolution mechanism of shale gas generation-storage-occurrence in MCTS, providing a quantitative framework for evaluating shale gas resources in transitional facies. The identified optimal conditions (moderate burial depth, balanced heat flow, and enriched TOC) offer guidance for targeting high-potential exploration zones in similar geological settings globally.

CRedit authorship contribution statement

Xiao-Guang Yang: Writing – original draft, Software, Methodology, Funding acquisition, Formal analysis, Data curation. **Shi-Zhen Li:** Supervision, Funding acquisition, Conceptualization. **Qiu-Chen Xu:** Writing – review & editing, Writing – original draft. **Fei Li:** Visualization, Software, Methodology. **Xiang-Lin Chen:** Writing – review & editing, Formal analysis.

Declaration of competing interest

The authors declare that they have no known competing financial interests or personal relationships that could have appeared to influence the work reported in this paper.

Acknowledgements

This study was financially supported by the National Natural Science Foundation of China (No. 42472210 and U25D9024), geological survey project of the China Geological Survey Oil and Gas Survey (No. [2024] 02-07-03), and the Grants-in-Aid of American Association of Petroleum Geologists (AAPG). The former two funds provided essential support for shale pore structure exploration and experimental works such as design, data collection, and analysis, while the AAPG Scholarship enabled international academic exchanges and cooperation, broadening the research perspective of the first author. Sincere gratitude is extended to all these supports.

References

- Athy, L.F., 1930. Density, porosity, and compaction of sedimentary rocks. AAPG Bull. 14, 1–24. <https://doi.org/10.1306/3D93289E-16B1-11D7-8645000102C1865D>.
- Borjigin, T., Lu, L.F., Yu, L.J., et al., 2021. Formation, preservation and connectivity control of organic pores in shale. Petrol. Explor. Dev. 48, 798–812. [https://doi.org/10.1016/S1876-3804\(21\)60067-8](https://doi.org/10.1016/S1876-3804(21)60067-8).
- Chalmers, G.R., Bustin, R.M., Power, I.M., 2012. Characterization of gas shale pore systems by porosimetry, pycnometry, surface area, and field emission scanning electron microscopy/transmission electron microscopy image analyses: Examples from the Barnett, Woodford, Haynesville, Marcellus, and Doig units. AAPG Bull. 96, 1099–1119. <https://doi.org/10.1306/1017111052>.

- Chen, L., Zuo, L., Jiang, Z., et al., 2019. Mechanisms of shale gas adsorption: evidence from thermodynamics and kinetics study of methane adsorption on shale. *Chem. Eng. J.* 361, 559–570. <https://doi.org/10.1016/j.cej.2018.11.185>.
- Chen, K., Yang, R., Bao, H., et al., 2023. Depositional-diagenetic process and their implications for pore development of Wufeng–Longmaxi shales in the Jiangdong block, Fuling shale gas field, SW China. *Mar. Petrol. Geol.* 151, 106177. <https://doi.org/10.1016/j.marpetgeo.2023.106177>.
- Curtis, J.B., 2002. Fractured shale-gas systems. *AAPG Bull.* 86, 1921–1938. <https://doi.org/10.1306/61EEDDBE-173E-11D7-8645000102C1865D>.
- Curtis, M.E., Sondergeld, C.H., Ambrose, R.J., et al., 2012. Microstructural investigation of gas shales in two and three dimensions using nanometer-scale resolution imaging. *AAPG Bull.* 96, 665–677. <https://doi.org/10.1306/08151110188>.
- Dong, T., Harris, N.B., Ayranci, K.A., et al., 2015. Porosity characteristics of the Devonian Horn River shale, Canada: Insights from lithofacies classification and shale composition. *Int. J. Coal Geol.* 141, 74–90. <https://doi.org/10.1016/j.coal.2015.03.001>.
- Fu, Y., Zhang, R., Jiang, Y., et al., 2023. Experimental studies on pore structure and the gas content evolution mechanisms of shale gas reservoirs at different burial depths in the Longmaxi Formation, Southern Sichuan Basin. *Appl. Sci.* 13, 13194. <https://doi.org/10.3390/app132413194>.
- Gai, H.F., Xiao, X.M., Cheng, P., et al., 2015. Gas generation of shale organic matter with different contents of residual oil based on a pyrolysis experiment. *Org. Geochem.* 78, 69–78. <https://doi.org/10.1016/j.orggeochem.2014.11.001>.
- Gasparik, M., Ghanizadeh, A., Gensterblum, Y., et al., 2013. “Multi-temperature” method for high-pressure sorption measurements on moist shales. *Rev. Sci. Instrum.* 84, 085116. <https://doi.org/10.1063/1.4817643>.
- Guo, Y., Huang, L., Li, X., 2023. Experimental investigation of the tensile behavior and acoustic emission characteristics of anisotropic shale under geothermal environment. *Energy* 263, 125767. <https://doi.org/10.1016/j.energy.2022.125767>.
- Guo, W., Deng, S., Sun, Y., 2024. Recent advances on shale oil and gas exploration and development technologies. *Adv. Geo. Energy Res.* 11, 81–87. <https://doi.org/10.46690/ager.2024.02.01>.
- Guo, X., Wang, R., Shen, B., et al., 2025. Geological characteristics, resource potential, and development direction of shale gas in China. *Petro. Exp. Develop.* 52 (1), 17–32. [https://doi.org/10.1016/S1876-3804\(25\)60002-4](https://doi.org/10.1016/S1876-3804(25)60002-4).
- Hakimi, M.H., Abdullah, W.H., Shalaby, M.R., 2010. Source rock characterization and oil generating potential of the Jurassic Madbi Formation, onshore East Shabawah oilfields, Republic of Yemen. *Org. Geochem.* 41, 513–521. <https://doi.org/10.1016/j.orggeochem.2009.12.011>.
- Han, Y., Horsfield, B., Wirth, R., et al., 2017. Oil retention and porosity evolution in organic-rich shales. *AAPG Bull.* 101, 807–827. <https://doi.org/10.1306/09221616069>.
- Hao, F., Zou, H., Lu, Y., 2013. Mechanisms of shale gas storage: Implications for shale gas exploration in China. *AAPG Bull.* 97, 1325–1346. <https://doi.org/10.1306/02141312091>.
- He, Q., Chen, S., Li, S., et al., 2022. Organic geochemical characteristics and hydrocarbon generation mechanism of marine-continental transitional organic-rich shale: A case study from the Shanxi Formation in the eastern margin of the Ordos Basin. *J. Petrol. Sci. Eng.* 219, 111116. <https://doi.org/10.1016/j.petrol.2022.111116>.
- Hu, X., Li, R., Ming, Y., et al., 2022. Insights into shale gas adsorption and an improved method for characterizing adsorption isotherm from molecular perspectives. *Chem. Eng. J.* 431, 134183. <https://doi.org/10.1016/j.cej.2021.134183>.
- Hu, Z., Klitzsch, N., Jin, Y., et al., 2023. Assessment of shale gas potential of marine-continental transitional Longtan Formation from Southwestern Guizhou Province, China. *Energy Fuels* 38, 387–401. <https://doi.org/10.1021/acs.energyfuels.3c04172>.
- Jarvie, D.M., Hill, R.J., Ruble, T.E., et al., 2007. Unconventional shale-gas systems: the Mississippian Barnett Shale of north-central Texas as one model for thermogenic shale-gas assessment. *AAPG Bull.* 91, 475–499. <https://doi.org/10.1306/1219060606068>.
- Jin, Z., Nie, H., 2022. Evolution history of overpressured and normally pressured shale gas reservoirs in Wufeng–Longmaxi formation, Sichuan Basin, China: An analysis from the perspective of source and seal coupling mechanism. *Energy Fuels* 36, 10870–10885. <https://doi.org/10.1021/acs.energyfuels.2c01925>.
- Kudryashov, N.A., 2015. Logistic function as solution of many nonlinear differential equations. *Appl. Math. Model.* 39, 5733–5742. <https://doi.org/10.1016/j.apm.2015.01.048>.
- Law, R., Murrell, D.J., Dieckmann, U., 2003. Population growth in space and time: Spatial logistic equations. *Ecology* 84, 252–262. [https://doi.org/10.1890/0012-9658\(2003\)084\[0252:PGISAT\]2.0.CO;2](https://doi.org/10.1890/0012-9658(2003)084[0252:PGISAT]2.0.CO;2).
- Lewan, M., Pawlewicz, M., 2017. Reevaluation of thermal maturity and stages of petroleum formation of the Mississippian Barnett Shale, Fort Worth Basin, Texas. *AAPG Bull.* 101, 1945–1970. <https://doi.org/10.1306/01251716053>.
- Li, Y., Guo, S., 2023. Sedimentary response and restoration of paleoshoreline of Taiyuan-Shanxi formations in North China Basin. *Mar. Petrol. Geol.* 152, 106218. <https://doi.org/10.1016/j.marpetgeo.2023.106218>.
- Li, X., Chen, G., Chen, Z., et al., 2016. An insight into the mechanism and evolution of shale reservoir characteristics with over-high maturity. *J. Nat. Gas Geosci.* 1, 373–382. <https://doi.org/10.1016/j.jnggs.2016.11.001>.
- Li, S.Z., Zhou, Z., Nie, L.F., et al., 2022. Distribution characteristics, exploration and development, geological theories research progress and exploration directions of shale gas in China. *China Geol.* 5, 110–135. <https://doi.org/10.31035/cg2021069>.
- Li, X., Du, W., Feng, X., et al., 2023. Pressure evolution mechanism of marine shale reservoirs and shale gas accumulation model: Evidence from fluid inclusions in the Wufeng–Longmaxi formations in the basin margin structural transition zone in northern Guizhou Province, China. *Minerals* 13, 241. <https://doi.org/10.3390/min13020241>.
- Li, M., Zhang, K., Meng, Z., et al., 2025. Evolution of thermodynamic behaviors of methane adsorption in variable migration pores of coals with different deformations. *Fuel* 396, 135346. <https://doi.org/10.1016/j.fuel.2025.135346>.
- Lis, G.P., Topór, T., Mastalerz, M., 2025. Organic matter content and its role in shale porosity development with maturity: Insights from Baltic Basin Silurian shales. *Int. J. Coal Geol.* 301, 104713. <https://doi.org/10.1016/j.coal.2025.104713>.
- Liu, B., Wang, Y., Tian, S., et al., 2022. Impact of thermal maturity on the diagenesis and porosity of lacustrine oil-prone shales: Insights from natural shale samples with thermal maturation in the oil generation window. *Int. J. Coal Geol.* 261, 104079. <https://doi.org/10.1016/j.coal.2022.104079>.
- Liu, J., Bai, X., Elsworth, D., 2024. Evolution of pore systems in low-maturity oil shales during thermal upgrading-quantified by dynamic SEM and machine learning. *Pet. Sci.* 21, 1739–1750. <https://doi.org/10.1016/j.petsci.2023.12.021>.
- Loucks, R.G., Reed, R.M., Ruppel, S.C., et al., 2009. Morphology, genesis, and distribution of nanometer-scale pores in siliceous mudstones of the Mississippian Barnett Shale. *J. Sediment. Res.* 79, 848–861. <https://doi.org/10.2110/jsr.2009.092>.
- Lu, C.G., Xiao, X.M., Xue, Z.Q., et al., 2024. Investigations of methane adsorption characteristics on marine-continental transitional shales and gas storage capacity models considering pore evolution. *Pet. Sci.* 21, 2273–2286. <https://doi.org/10.1016/j.petsci.2024.03.027>.
- Ma, L., Yu, Q., 2020. Dynamic behaviors of methane adsorption on partially saturated shales. *J. Petrol. Sci. Eng.* 190, 107071. <https://doi.org/10.1016/j.petrol.2020.107071>.
- Ma, W., Cao, Y., Xi, K., et al., 2022. Interactions between mineral evolution and organic acids dissolved in bitumen in hybrid shale system. *Int. J. Coal Geol.* 260, 104071. <https://doi.org/10.1016/j.coal.2022.104071>.
- Merkel, A., Fink, R., Littke, R., 2016. High pressure methane sorption characteristics of lacustrine shales from the Midland Valley Basin, Scotland. *Fuel* 182, 361–372. <https://doi.org/10.1016/j.fuel.2016.05.118>.
- Miao, H., Jiang, Z., Tang, G., et al., 2023. Strata uplift controlled deep shale gas accumulation modes: A case study from the Weiyuan block, Sichuan Basin. *Energy Fuels* 37, 12889–12904. <https://doi.org/10.1021/acs.energyfuels.3c02255>.
- Mohamed, N.S., El, N., Mohamed, M., 2016. Utilizing the Rock-Eval pyrolysis and biomarkers parameters to characterize the organic matters of selected wells in the Central Gulf of Suez, Egypt. *Energy sources Part A Recovery utilization. Environ. Effects* 38, 3158–3166. <https://doi.org/10.1080/15567036.2016.1141270>.
- Mondol, N.H., Bjørlykke, K., Jahren, J., et al., 2007. Experimental mechanical compaction of clay mineral aggregates—Changes in physical properties of mudstones during burial. *Mar. Petrol. Geol.* 24, 289–311.
- Myers, A., Monson, P., 2002. Adsorption in porous materials at high pressure: Theory and experiment. *Langmuir* 18, 10261–10273. <https://doi.org/10.1016/j.marpetgeo.2007.03.006>.
- Nie, H., Dang, W., Zhang, Q., et al., 2024. Evaluation of gas content in organic-rich shale: A review of the history, current status, and future directions. *Geosci. Front.* 15, 101921. <https://doi.org/10.1016/j.gsf.2024.101921>.
- Pan, C.C., Jiang, L.L., Liu, J.Z., et al., 2012. The effects of pyrobitumen on oil cracking in confined pyrolysis experiments. *Org. Geochem.* 45, 29–47. <https://doi.org/10.1016/j.orggeochem.2012.01.008>.
- Pan, B., Li, Y., Zhang, X., et al., 2020. Effect of total organic carbon (TOC) content on shale wettability at high pressure and high temperature conditions. *J. Petrol. Sci. Eng.* 193, 107374. <https://doi.org/10.1016/j.petrol.2020.107374>.
- Pang, X., Li, M., Li, S., et al., 2005. Geochemistry of petroleum systems in the Niuzhuang South slope of Bohai Bay Basin: Part 3. Estimating hydrocarbon expulsion from the Shahejie Formation. *Org. Geochem.* 36, 497–510. <https://doi.org/10.1016/j.orggeochem.2004.12.001>.
- Park, S.Y., Liang, Y., 2016. Biogenic methane production from coal: A review on recent research and development on microbially enhanced coalbed methane (MECBM). *Fuel* 166, 258–267. <https://doi.org/10.1016/j.fuel.2015.10.121>.
- Peters, K.E., 1986. Guidelines for evaluating petroleum source rock using programmed pyrolysis. *AAPG Bull.* 70, 318–329. <https://doi.org/10.1306/94885688-1704-11D7-8645000102C1865D>.
- Setzmann, U., Wagner, W., 1991. A new equation of state and tables of thermodynamic properties for methane covering the range from the melting line to 625 K at pressures up to 1000 MPa. *J. Phys. Chem. Ref. Data* 20, 1061–1155. <https://doi.org/10.1063/1.555898>.

- Sweeney, J.J., Burnham, A.K., 1990. Evaluation of a simple model of vitrinite reflectance based on chemical kinetics. *AAPG Bull.* 74, 1559–1570. <https://doi.org/10.1306/0C9B251F-1710-11D7-8645000102C1865D>.
- Tang, X., Yang, S., Hu, S., 2018. Thermal-history reconstruction of the Baiyun Sag in the deep-water area of the Pearl River Mouth Basin, northern South China Sea. *Front. Earth Sci.* 12, 532–544. <https://doi.org/10.1007/s11707-017-0675-7>.
- Tang, X., Jiang, Z., Jiang, S., et al., 2021. Structure, burial, and gas accumulation mechanisms of lower Silurian Longmaxi Formation shale gas reservoirs in the Sichuan Basin (China) and its periphery. *AAPG Bull.* 105, 2425–2447. <https://doi.org/10.1306/0702211610418010>.
- Tian, H., Xiao, X.M., Wilkins, R.W.T., et al., 2012. An experimental comparison of gas generation from three oil fractions: Implications for the chemical and stable carbon isotopic signatures of oil cracking gas. *Org. Geochem.* 46, 96–112. <https://doi.org/10.1016/j.orggeochem.2012.01.013>.
- Tian, H., Li, T., Zhang, T., et al., 2016. Characterization of methane adsorption on overmature Lower Silurian–Upper Ordovician shales in Sichuan Basin, southwest China: Experimental results and geological implications. *Int. J. Coal Geol.* 156, 36–49. <https://doi.org/10.1016/j.coal.2016.01.013>.
- Varma, A.K., Mishra, D.K., Samad, S.K., et al., 2018. Geochemical and organo-petrographic characterization for hydrocarbon generation from Barakar Formation in Auranga Basin, India. *Int. J. Coal Geol.* 186, 97–114. <https://doi.org/10.1016/j.coal.2017.12.002>.
- Wang, G., Jin, Z., Zhang, Q., et al., 2023. Effects of clay minerals and organic matter on pore evolution of the early mature lacustrine shale in the Ordos Basin, China. *J. Asian Earth Sci.* 246, 105516. <https://doi.org/10.1016/j.jseaeas.2022.105516>.
- Wu, G.C., Baleanu, D., 2014. Discrete fractional logistic map and its chaos. *Nonlinear Dyn.* 75, 283–287. <https://doi.org/10.1007/s11071-013-1065-7>.
- Xiao, X.M., Zeng, Q.H., Tian, H., et al., 2005. Origin and accumulation model of the AK-1 natural gas pool from the Tarim Basin, China. *Org. Geochem.* 36, 1285–1298. <https://doi.org/10.1016/j.orggeochem.2005.04.001>.
- Xie, X., Volkman, J.K., Qin, J., et al., 2014. Petrology and hydrocarbon potential of microalgal and macroalgal dominated oil shales from the Eocene Huadian Formation, NE China. *Int. J. Coal Geol.* 124, 36–47. <https://doi.org/10.1016/j.coal.2013.12.013>.
- Xie, W., Chen, S., Vandeginste, V., et al., 2022. Review of the effect of diagenetic evolution of shale reservoir on the pore structure and adsorption capacity of clay minerals. *Energy Fuels* 36, 4728–4745. <https://doi.org/10.1021/acs.energyfuels.2c00675>.
- Xin, D., Zhang, S.H., Tang, S.H., et al., 2023. Influence of rock properties and prediction on the methane storage capacity in marine-continental transitional shale and coal from Northern China. *J. Asian Earth Sci.* 254, 105740. <https://doi.org/10.1016/j.jseaeas.2023.105740>.
- Yang, X.G., Guo, S.B., 2020. Porosity model and pore evolution of transitional shales: An example from the Southern North China Basin. *Pet. Sci.* 17, 1512–1526. <https://doi.org/10.1007/s12182-020-00481-7>.
- Yang, X.G., Guo, S.B., 2021. Reservoirs characteristics and environments evolution of lower permian transitional shale in the Southern North China Basin: Implications for shale gas exploration. *J. Nat. Gas Sci. Eng.* 96, 104282. <https://doi.org/10.1016/j.jngse.2021.104282>.
- Yang, X.G., Guo, S.B., 2022. Gas content evolution in western Guizhou and differential occurrence in China of Permian shale with type III kerogen. *J. Pet. Sci. Eng.* 208, 109464. <https://doi.org/10.1016/j.petrol.2021.109464>.
- Yang, R., He, S., Hu, Q., et al., 2016. Pore characterization and methane sorption capacity of over-mature organic-rich Wufeng and Longmaxi shales in the southeast Sichuan Basin, China. *Mar. Petrol. Geol.* 77, 247–261. <https://doi.org/10.1016/j.marpetgeo.2016.06.001>.
- Yang, R., Hu, Q., He, S., et al., 2019. Wettability and connectivity of overmature shales in the Fuling gas field, Sichuan Basin (China). *AAPG Bull.* 103, 653–689. <https://doi.org/10.1306/09051817138>.
- Yu, Z., Wang, Z., Fan, W., et al., 2022. Evaluating the sedimentological and diagenetic impacts on terrestrial lacustrine fan delta sandy conglomerates reservoir quality: Insights from the Triassic Baikouquan Formation in the Mahu sag, Junggar Basin, Western China. *Mar. Petrol. Geol.* 146, 105973. <https://doi.org/10.1016/j.marpetgeo.2022.105973>.
- Zhang, J., Wei, C., Zhao, C., et al., 2021. Effects of nano-pore and macromolecule structure of coal samples on energy parameters variation during methane adsorption under different temperature and pressure. *Fuel* 289, 119804. <https://doi.org/10.1016/j.fuel.2020.119804>.
- Zhang, J., Shi, M., Wang, D., et al., 2022. Fields and directions for shale gas exploration in China. *Nat. Gas. Ind. B* 9, 20–32. <https://doi.org/10.1016/j.ngib.2021.08.014>.
- Zhang, K., Xi, Z., Zhang, S., et al., 2025. Characteristics of organic matter types and organic matter pore development in marine-continental transitional shale. *Geol. J. Early View*. <https://doi.org/10.1002/gj.5160>.
- Zou, C., 2024. Unveiling the oldest industrial shale gas reservoir: Insights for the enrichment pattern and exploration direction of Lower Cambrian shale gas in the Sichuan Basin. *Engineering* 42, 278–294. <https://doi.org/10.1016/j.eng.2024.03.007>.